



Article

Algorithm for the Reconstruction of the Ground Surface Reflectance in the Visible and Near IR Ranges from MODIS Satellite Data with Allowance for the Influence of Ground Surface Inhomogeneity on the Adjacency Effect and of Multiple Radiation Reflection

Mikhail V. Tarasenkov ^{1,*} , Vladimir V. Belov ¹ , Marina V. Engel ¹, Anna V. Zimovaya ¹, Matvei N. Zonov ^{1,2} and Alexandra S. Bogdanova ¹

¹ V.E. Zuev Institute of Atmospheric Optics SB RAS, 1, Academician Zuev Square, 634055 Tomsk, Russia

² Sobolev Institute of Mathematics, 4, Acad. Koptyug Ave., 630090 Novosibirsk, Russia

* Correspondence: tmv@iao.ru



Citation: Tarasenkov, M.V.; Belov, V.V.; Engel, M.V.; Zimovaya, A.V.; Zonov, M.N.; Bogdanova, A.S. Algorithm for the Reconstruction of the Ground Surface Reflectance in the Visible and Near IR Ranges from MODIS Satellite Data with Allowance for the Influence of Ground Surface Inhomogeneity on the Adjacency Effect and of Multiple Radiation Reflection. *Remote Sens.* **2023**, *15*, 2655. <https://doi.org/10.3390/rs15102655>

Academic Editors: Cédric Jamet, Federico Santini and Angelo Palombo

Received: 13 April 2023

Revised: 12 May 2023

Accepted: 16 May 2023

Published: 19 May 2023



Copyright: © 2023 by the authors. Licensee MDPI, Basel, Switzerland. This article is an open access article distributed under the terms and conditions of the Creative Commons Attribution (CC BY) license (<https://creativecommons.org/licenses/by/4.0/>).

Abstract: An atmospheric correction algorithm is proposed for the reconstruction of the ground surface reflectance from the data of satellite measurements. A distinctive feature of the algorithm is that it takes into account the influence of the ground surface inhomogeneity on the adjacency effect and additional illumination of the ground surface by reflected radiation. These factors are important for the reconstruction of the reflectance of ground surface fragments with sharp reflectance changes and high atmospheric turbidity. The algorithm is based on Monte Carlo programs developed by the authors. To reduce the computing time, we have proposed some original criteria and approaches. To estimate the capabilities of the developed algorithm, its results have been validated by comparing with the results of the MOD09 algorithm for four MODIS bands and measurements for the Portugal surface fragment with coordinates 38.829 N, 8.791 W. Good agreement of the results obtained by the proposed algorithm with the surface measurements and the data obtained by the MOD09 algorithm demonstrates the efficiency of the proposed algorithm in the reconstruction of the ground surface reflectance.

Keywords: satellite images; atmospheric correction; ground surface reflectance; MODIS data; Monte Carlo method

1. Introduction

Algorithms for retrieving the ground surface reflectance from satellite measurements have been developed for more than four decades, starting from such studies as [1]. To date, there are dozens of ways for solving this problem. The algorithms based on the solution of the radiative transfer equation (RTE) are referred to as radiative transfer model (RTM) algorithms. Algorithms are developed for satellite sensing of both land and water surfaces. The material presented below is primarily related to the problem of land sensing under conditions of a cloudless atmosphere. The problem solution for the water surface has its own specificity. The reflection from water surfaces is considered specular, in contrast to most land surfaces. According to [2], the received radiance in ocean remote sensing consists of: (1) radiation that did not interact with the water surface, (2) specularly reflected solar radiation, (3) radiation reflected by foam and whitecaps, and (4) radiation scattered by the upper water layer. Water surfaces are horizontally more uniform than land areas. Therefore, water surface can be treated as horizontally uniform when inverse problems of sensing are solved. In general, the state-of-the-art in algorithms for sensing of water surfaces can be judged from [2–5]. According to [6], a signal received by a satellite receiver in the visible and near-IR ranges can be divided into the following components (Figure 1): (1) radiation

that does not interact with the ground surface (Figure 1a), (2) direct solar radiation that interacts with the surface fragment under study (Figure 1b), (3) diffuse solar radiation that interacts with the surface fragment under study (Figure 1c), (4) adjacency effect (AE) due to single reflected radiation (Figure 1d), and (5) adjacency effect due to multiple reflected radiation (Figure 1e).

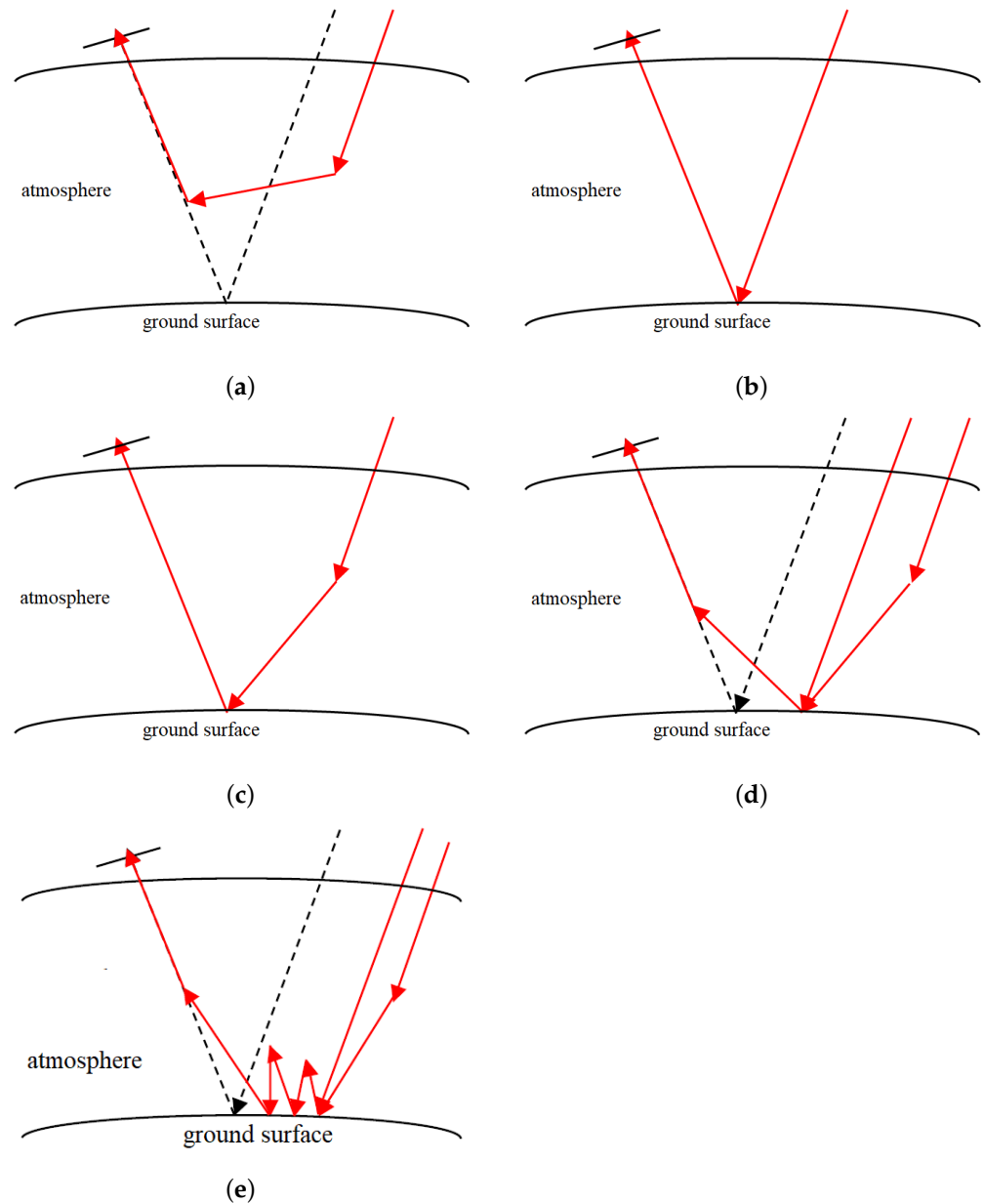


Figure 1. Optical fluxes forming the received radiation (according to [6]): (a) radiation that does not interact with the ground surface; (b) direct solar radiation that interacts with the surface fragment under study; (c) diffuse solar radiation that interacts with the surface fragment under study; (d) adjacency effect (AE) due to single reflected radiation; (e) adjacency effect due to multiple reflected radiation.

However, the solution of the system of equations without additional simplifications is very time-consuming. Thus, this approach is hard to apply to actual satellite data. That is why similar problems in later studies were solved with some simplifications reducing the computer time needed to obtain the desired solutions. RTM algorithms differ in the way of considering the following factors: (1) non-Lambertian character of the surface, (2) adjacency effect, (3) multiple reflection, (4) absorption, (5) radiation polarization, and (6) surface

topography. Table 1 compares some RTM algorithms for retrieval of the surface reflectance considering/ignoring the factors affecting the radiative transfer.

Table 1. RTM algorithms for retrieval of the surface reflectance.

Factor	Authors/Reference							
	Putsay [7]	Tanre [6]	Berk [8]	Vermote [9]	Lyapustin [10]	Reinersman [11]	Katkovskiy [12]	Shi [13]
Surface model	Lamb	Non-Lamb	Lamb	Non-Lamb	Non-Lamb	Lamb	Lamb	Non-Lamb
Adjacency effect	accurate	accurate	approx.	approx.	accurate	accurate	approx.	approx.
Multiple reflection	No	approx.	approx.	approx.	approx.	approx.	approx.	approx.
Molecular absorption	accurate	accurate	accurate	accurate	accurate	accurate	approx.	accurate
Polarization	No	No	No	Yes	Yes	No	No	No
Topography	No	No	No	No	No	No	No	Yes

It can be seen from Table 1 that some algorithms employ the approximate Lambertian surface model, while others consider accurately the non-Lambertian character of the surface, usually, after the solution of the problem in the Lambertian approximation. Many algorithms take into account the adjacency effect approximately. They assume that the point spread function (PSF) of the AE is axisymmetric or that the surface around an observed pixel is uniform. For example, it is shown in p. 34 of [9] that PSF of the AE is significantly non-axisymmetric in azimuth if the optical axis of the receiver system is tilted by 70° about nadir. All the studies analyzed in Table 1 either ignore the multiple reflection or assume that the surface around the observed pixel is uniform. However, it is stated in some papers (for example, in [14]) that the consideration of multiple reflection may be important for situations of a sharp transition from a low reflective surface to a high reflective surface. In some papers, molecular absorption is taken into account separately from scattering, which may be unacceptable in the case of a significant influence of multiple scattering. The radiation polarization is also ignored in many studies. However, for example, our estimates in [15] have shown that this factor may be important for the solution of the inverse problem under consideration. According to [16], ignoring the effects of polarization leads to the following errors in calculated top-of-atmosphere reflectances: more than 10% for a molecular atmosphere and up to 5% for an aerosol atmosphere. If there is a large height difference in the observed surface, then topography can also be an important factor affecting the results of solution. Most papers considering topography ignore the radiation extinction and the adjacency effect. It should be emphasized that, in a cloudy atmosphere, it is often unacceptable to ignore the adjacency effect from clouds in approaches to the interpretation of the data of passive satellite sensing of the ground surface under the conditions of a cloudless atmosphere that are described in [6–13]. The adjacency effect from clouds is studied, for example, in [17–21]. The algorithms considered in Table 1 and similar ones have formed the basis for several software packages: ATCOR [22], ACORN [23], ATREM [24], FLAASH [25], HATCH [26], and others. Nevertheless, the problem of correct estimation of surface reflectance from satellite data is not completely solved yet.

In [27], we have proposed the algorithm for retrieving the ground surface reflectances observed through the cloudless atmosphere. This algorithm allows accurate consideration of the adjacency effect, multiple reflection of the radiation from the surface, and the radiation polarization. In this paper, this algorithm is validated against the MODIS data and the ground-based measurements in Portugal [28]. The results obtained with our algorithm are compared with the MOD09 results.

2. Algorithm for Retrieval of the Surface Reflectance

2.1. Assumptions and Problem Formulation

When developing the algorithm for retrieval of surface reflectance r_{surf} , we have assumed the following:

1. The atmosphere is a scattering and absorbing aerosol-gas medium.
2. The atmosphere is cloudless and vertically stratified into 32 uniform layers.
3. The “atmosphere-ground surface” system is spherical, and refraction is ignored. The boundaries of the atmospheric layers are spheres.
4. The source of radiation is the sun. There are no other sources.
5. The ground surface is non-uniform and reflects radiation according to the Lambert law.
6. The ground surface is uniform within a pixel.
7. Local topography is ignored.
8. The change in the illumination of the ground surface due to a change in the solar zenith angle is negligibly small.
9. The radiative transfer is considered in the monochromatic approximation.

According to the algorithm [29], the non-Lambertian character of the ground surface can be taken into account once the ground surface reflectances r_{surf} are determined in the approximation of Lambertian reflection. The most common way to take into account the non-Lambertian character of the surface is by using the Ross–Thick–Li–Spars model [30]. Alternative BRDF models were presented in works [31–35]. The analysis of earlier publications shows that the simultaneous consideration of surface topography and reflection inhomogeneity was not performed in the solution of the inverse problem. Knowing surface slopes (from, for example, Ref. [36]), we can normalize the surface before performing the atmospheric correction or use corrections for surface topography in the systems of equations to be solved.

Let the task be to determine surface reflectances for the considered fragment of the ground surface from radiance measured by a satellite receiver.

2.2. System of Equations to Be Solved

In the above assumptions, the algorithm is based on the decomposition of the radiance measured by a satellite receiver into the following components:

$$I_r(\varphi_{N,ij}, \lambda_{N,ij}, \mu_{sun}, \mu_{d,ij}, \alpha_{ij}) = I_{atm}(\mu_{sun}, \mu_{d,ij}, \alpha_{ij}) + I_0(\varphi_{N,ij}, \lambda_{N,ij}, \mu_{sun}, \mu_{d,ij}) + I_{surf,sc}(\varphi_{N,ij}, \lambda_{N,ij}, \mu_{sun}, \mu_{d,ij}) \quad (1)$$

where I_{atm} is the radiance of the flux non-interacting with the ground surface (Figure 1a); I_0 is the radiance of the flux reflected from the surface that reached the receiver without scattering upon the reflection (Figure 1b,c); $I_{surf,sc}$ is the radiance of the flux reflected from the ground surface that reached the receiver after scattering (Figure 1d,e); $\varphi_{N,ij}$, $\lambda_{N,ij}$ are the coordinates of the center of the observed pixel in the i -th line and j -th column of the considered fragment; μ_{sun} is the cosine of the solar zenith angle; μ_d is the cosine of the zenith angle of the receiving system; and α is the relative azimuth angle between the directions to the satellite and to the sun at the observed surface point.

Within the framework of the above assumptions, the value of I_0 can be found as

$$I_0(\varphi_{N,ij}, \lambda_{N,ij}, \mu_{sun}, \mu_{d,ij}) = r_{surf}(\varphi_{N,ij}, \lambda_{N,ij}) E_{sum}(\varphi_{N,ij}, \lambda_{N,ij}, \mu_{sun}) \frac{1}{\pi} \exp(-\tau(\mu_{d,ij})), \quad (2)$$

where E_{sum} is the total irradiance at the surface point and τ is the optical thickness of the path from the observed surface point to the receiver.

In the above assumptions, the value of $I_{surf,sc}$ can be determined as

$$\begin{aligned}
& I_{surf,sc}(\varphi_{N,ij}, \lambda_{N,ij}, \mu_{sun}, \mu_{d,ij}) \\
&= \sum_{k=1}^{N_i} \sum_{l=1}^{N_j} r_{surf}(\varphi_{N,kl}, \lambda_{N,kl}) E_{sum}(\varphi_{N,kl}, \lambda_{N,kl}, \mu_{sun}) h(\rho_{w,ijkl}, \alpha_{w,ijkl}, \mu_{d,ij}) S_{kl} \\
& \quad + \bar{Q} A_{out}(\varphi_{N,ij}, \lambda_{N,ij}), \quad (3)
\end{aligned}$$

$$A_{out}(\varphi_{N,ij}, \lambda_{N,ij}) = \iint_S h(\rho_w, \alpha_w, \mu_{d,ij}) dS - \sum_{k=1}^{N_i} \sum_{l=1}^{N_j} h(\rho_{w,ijkl}, \alpha_{w,ijkl}, \mu_{d,ij}) S_{kl} \quad (4)$$

where S_{kl} is the area of the pixel in the k -th line and l -th column of the considered fragment; $\rho_{w,ijkl}$ is the distance from the point with coordinates $\varphi_{N,ij}, \lambda_{N,ij}$ to the point with coordinates $\varphi_{N,kl}, \lambda_{N,kl}$ along the earth's surface; $\alpha_{w,ijkl}$ is the relative azimuthal angle at the point with coordinates $\varphi_{N,ij}, \lambda_{N,ij}$ between the direction to the receiving system and to the point with coordinates $\varphi_{N,kl}, \lambda_{N,kl}$; ρ_w, α_w are the surface polar coordinates on the spherical ground surface from the observed point; h is PSF of the AE, $1/(\text{m}^2 \text{sr})$; dS is the differential over the ground surface; and \bar{Q} the average luminosity of the considered surface fragment in the approximation of the uniform surface, $W/(\text{m}^2 \mu\text{m})$. The first term on the right side in the Equation (3) estimates the adjacency effect from the considered area of the ground surface. The second term on the right side in the Equation (3) estimates the adjacency effect from regions outside the considered area of the ground surface.

It is proposed to determine the total irradiance of the ground surface E_{sum} with allowance for the additional irradiance due to multiple reflected radiation by the following equation:

$$\begin{aligned}
E_{sum}(\varphi_{N,ij}, \lambda_{N,ij}, \mu_{sun}) = E_0(\mu_{sun}) + E_0(\mu_{sun}) \sum_{k=1}^{N_i} \sum_{l=1}^{N_j} r_{surf}(\varphi_{N,kl}, \lambda_{N,kl}) h_1(\rho_{w,ijkl}) S_{kl} \\
+ C_{out}(\varphi_{N,ij}, \lambda_{N,ij}) \overline{r_{surf}} + E_0(\mu_{sun}) \frac{(\overline{r_{surf}} \gamma_1)^2}{1 - \overline{r_{surf}} \gamma_1} \quad (5)
\end{aligned}$$

$$C_{out}(\varphi_{N,ij}, \lambda_{N,ij}) = \gamma_1 - \sum_{k=1}^{N_i} \sum_{l=1}^{N_j} h_1(\rho_{w,ijkl}) S_{kl} \quad (6)$$

$$\gamma_1 \equiv 2\pi \int_0^{\pi R_e} h_1(\rho_w) d\rho_w$$

where E_0 is the irradiance of the ground surface for a non-reflective ground surface, $W/(\text{m}^2 \mu\text{m})$; h_1 is PSF of the additional surface irradiance formation, $1/\text{m}^2$; γ_1 is the integral of the function h_1 over the entire ground surface; $d\rho_w$ is the differential of the distance over the spherical ground surface; and R_e is the Earth radius. The first term on the right side of the Equation (5) characterizes the irradiance of the ground surface by non-reflected radiation. The second term describes additional irradiance by radiation singly reflected from the points of the area under consideration. The third term gives the additional irradiance by radiation singly reflected outside the area under consideration. The fourth term describes the additional irradiance by reflected radiation with a reflection multiplicity of two or more.

Most alternative algorithms for retrieval of surface reflectance (for example, [9,10]) employ the simplified equation

$$E_{sum}(\varphi_{N,ij}, \lambda_{N,ij}, \mu_{sun}) = \frac{E_0(\mu_{sun})}{1 - \overline{r_{surf}} \gamma_1} \quad (7)$$

in place of Equation (5). In Equation (7), $\overline{r_{surf}}$ is the reflectance averaged over the observed surface fragment in the approximation of the uniform surface.

According to our calculations, the upper estimate of the error of using Equation (7) is $\Delta_1 = \frac{r_{surf,max}\gamma_1}{1-r_{surf,max}\gamma_1}$, while that for Equation (5) is $\Delta_2 = \frac{(r_{surf,max}\gamma_1)^2}{1-r_{surf,max}\gamma_1}$, ($r_{surf,max}$ is the maximal value of the surface reflectance over the considered surface fragment). For example, for the situation $r_{surf} < 0.4$, we have obtained $\Delta_1 \leq 0.106$ and $\Delta_2 \leq 0.01$ for the molecular atmosphere in the visible wavelength range and $\Delta_1 \leq 0.19$ and $\Delta_2 \leq 0.03$ for the high atmospheric turbidity ($AOD_{0.55} = 7.0$). Thus, in the limiting situations, the use of Equation (7) may yield an unacceptably high error (up to 19% of the total surface irradiance). At the same time, the consideration of the inhomogeneity of surface reflection in the double reflected radiation allows this error to be decreased down to below 3%. A description of how this assessment was made has been added to the Supplementary Materials [37].

With allowance for Equations (1)–(5), the solution of the problem is divided into two stages:

(1) Determination of the surface luminosity $Q = r_{surf}E_{sum}$ from the system of linear equations

$$I_r(\varphi_{N,ij}, \lambda_{N,ij}, \mu_{sun}, \mu_{d,ij}, \alpha_{ij}) - I_{atm}(\mu_{sun}, \mu_{d,ij}, \alpha_{ij}) = Q(\varphi_{N,ij}, \lambda_{N,ij}, \mu_{sun}) \frac{1}{\pi} \exp(-\tau(\mu_{d,ij})) + \sum_{k=1}^{N_i} \sum_{l=1}^{N_j} Q(\varphi_{N,kl}, \lambda_{N,kl}, \mu_{sun}) h(\rho_{w,ijkl}, \alpha_{w,ijkl}, \mu_{d,ij}) S_{kl} + \bar{Q}A_{out}(\varphi_{N,ij}, \lambda_{N,ij}) \quad (8)$$

(2) Determination of the surface reflectance from the system of nonlinear equations

$$Q(\varphi_{N,ij}, \lambda_{N,ij}, \mu_{sun}) = r_{surf}(\varphi_{N,ij}, \lambda_{N,ij})E_0(\mu_{sun}) \times \left(1 + \sum_{k=1}^{N_i} \sum_{l=1}^{N_j} r_{surf}(\varphi_{N,kl}, \lambda_{N,kl}) h_1(\rho_{w,ijkl}) S_{kl} + C_{out}(\varphi_{N,ij}, \lambda_{N,ij}) \overline{r_{surf}} + \frac{(r_{surf}\gamma_1)^2}{1-r_{surf}\gamma_1} \right) \quad (9)$$

In general, the above Equations (1)–(3) are similar, with the exception of some minor details, to the equations from works [6–13]. The closest approach is in [11]. Equation (5), used in the present algorithm, is usually not used. Instead, Equation (7) is most often used. Moreover, several additional simplifications to reduce the computational time are considered below.

2.3. Additional Simplifications to Reduce the Computation Time

Systems of Equations (8) and (9) have the following features: (i) if the functions h and h_1 are calculated separately for every pixel, then the computation takes a huge time for a large surface fragment (hundreds of thousands of pixels or more), (ii) summation over all image lines and columns yields the systems with constants having the dimension of $(N_i \times N_j)^2$, which makes systems (8) and (9) of little use, (iii) the calculation of I_{atm} for every pixel also takes a lot of computing time, (iv) pixels may be arranged unevenly over the ground surface—therefore, an algorithm is needed to determine quickly the areas of fragments closest to the center of a given pixel S_{kl} . To solve these problems, we have proposed some methods [27,38] that are described below.

2.3.1. Use of Isoplanar Zones

To avoid calculation of h for every pixel separately, it is proposed to divide the surface fragment, for which the reflectances are retrieved, into zones, within which the function h can be considered constant in the variable μ_d with some given error δ . It is obvious that the function h is the same at the fixed angle θ_d of deviation from the nadir direction and the arbitrary azimuth angle. Therefore, isoplanar zones (zones, where h is the same) should be limited to rings with some constant angles of deviation from the nadir direction. Alternative algorithms (e.g., Ref. [9]) often use the axisymmetric function h obtained in

nadir observations instead. To set the boundaries of isoplanar zones, we propose to use the recurrent equation [38]:

$$\begin{cases} H(\mu_k) = H(1) - C(1 - \mu_k)^N \\ \mu_{k+1} = 1 - \left[\frac{1}{C} \left(H(1) - \frac{H(\mu_k)}{1 + \delta} \right) \right]^{1/N} \end{cases} \tag{10}$$

$$H(\mu_k) \equiv \frac{1}{\pi} \exp(-\tau(\mu_k)) + \iint_S h(\rho_w, \alpha_w, \mu_k) dS \tag{11}$$

$$\mu_k \equiv \cos\theta_k$$

The use of Equation (10) is justified in the Supplementary Materials [37].

2.3.2. Use of the Adjacency Effect Radius

The system of Equation (8) includes the terms responsible for the adjacency effect (AE) from all zones of the observed surface fragment. However, PSF of the AE is a rapidly decreasing function. Therefore, for any h , we can set (with some error) the AE radius R_k , outside which the adjacency effect can be considered equal to 0. Each isoplanar zone has its own radius R_k . We set R_k so that the approximate surface luminosity \tilde{Q} differs from the exact value of Q by smaller than the preset discrepancy δ_1 , that is,

$$1 \geq \min_{i,j} \frac{Q_{ij}}{\tilde{Q}_{ij}} \geq \delta_1. \tag{12}$$

Condition (12) is based on the fact that summation of only terms within R_k in Equation (8) overestimates the value of Q . It can be shown that, to fulfill condition (12), it is sufficient to fulfill the condition on the AE radius R_k :

$$k_1(R_k) \equiv \frac{\iint_{S(R_k)} h(\rho_w, \alpha_w, \mu_k) dS}{\iint_S h(\rho_w, \alpha_w, \mu_k) dS} \geq \delta_1 + (\delta_1 - 1) \frac{\frac{1}{\pi} \exp(-\tau(\mu_k))}{\iint_S h(\rho_w, \alpha_w, \mu_k) dS}, \tag{13}$$

where $S(R_k)$ is the region on a spherical earth’s surface bounded by a radius R_k . The use of Equation (13) is justified in the Supplementary Materials [37].

Then, with known R_k , for each isoplanar zone, for any pixel we can find the range of lines k and columns l limiting the AE radius. Alternative algorithms considering the adjacency effect (for example, [9]) often use the fixed number of lines and columns for all situations, which ignores the dependence of R_k on the state of the atmosphere and μ_d .

2.3.3. Use of the Radius of Effect of Single Reflection on Ground Surface Illumination

In the sums over k and l in nonlinear system of Equation (9), we propose to remain only terms inside the radius of formation of additional irradiance R_S . To set R_S , we impose the condition that the error in determining r_{surf} does not exceed δ_2 :

$$1 \geq \min_{i,j} \frac{r_{surf,ij}}{\tilde{r}_{surf,ij}} \geq \delta_2. \tag{14}$$

Condition (14) is reasoned by the fact that the use of R_S overestimates r_{surf} . It can be shown (Supplementary Materials [37]) that, for condition (14) to be true, it is sufficient to satisfy the following condition:

$$k_2(R_S) \equiv \frac{2\pi \int_0^{R_S} h_1(\rho_w) d\rho_w}{\gamma_1} \geq \frac{\delta_2}{\gamma_1} \left(\frac{\delta_2}{1 - \gamma_1} - 1 \right), \tag{15}$$

Then, with known R_S , for each pixel we can find the range of lines k and columns l limiting the radius of formation of additional irradiance.

2.3.4. Use of Approximations for I_{atm}

The value of I_{atm} depends on three variables characterizing the mutual position of the sun and the receiver μ_{sun}, μ_d and α . If the surface fragment, for which atmospheric correction is performed, is small, then I_{atm} can be considered as approximately constant. Otherwise, instead of calculating this value for each location of the receiver and the sun, it is proposed to use the approximation formula

$$I_{atm}(\mu_{sun}, \mu_d, \alpha) = -\frac{B(\mu_d, \alpha) + \sqrt{B(\mu_d, \alpha)^2 - 4A(\mu_d, \alpha)C_{13}}}{2A(\mu_d, \alpha)\mu_d}, \quad (16)$$

$$A(\mu_d, \alpha) = \begin{cases} C_{11} \mu_d^2 + C_{21} \left(\sqrt{1 - \mu_d^2} \cos \alpha \right)^2 + C_{22} \mu_d \sqrt{1 - \mu_d^2} \cos \alpha - \left(\sqrt{1 - \mu_d^2} \sin \alpha \right)^2, & \alpha \leq 90^\circ \\ C_{11} \mu_d^2 + C_{31} \left(\sqrt{1 - \mu_d^2} \cos \alpha \right)^2 + C_{32} \mu_d \sqrt{1 - \mu_d^2} \cos \alpha - \left(\sqrt{1 - \mu_d^2} \sin \alpha \right)^2, & \alpha > 90^\circ \end{cases} \quad (17)$$

$$B(\mu_d, \alpha) = \begin{cases} C_{12} \mu_d + C_{23} \sqrt{1 - \mu_d^2} \cos \alpha, & \alpha \leq 90^\circ \\ C_{12} \mu_d + C_{33} \sqrt{1 - \mu_d^2} \cos \alpha, & \alpha > 90^\circ \end{cases} \quad (18)$$

where $C_{11}, C_{12}, C_{13}, C_{21}, C_{22}, C_{23}, C_{31}, C_{32}, C_{33}$ are the approximation constants. The approximation constants are determined by the least-square fit method from the values of I_{atm} calculated by the Monte Carlo method for given μ_{sun} and the atmospheric model, as well as for $\mu_d = 1, 0.996, \dots, 0.259$ and $\alpha = 0, 10, \dots, 180^\circ$.

The use of approximation (16) is justified in the Supplementary Materials [37]. The use of approximation (16) for the situations considered below has an error no more than 1.5% for MODIS bands 1, 3, and 4 and no more than 3% for MODIS band 2. This leads to the absolute errors in retrieval of r_{surf} no higher than 7×10^{-4} for band 1, 7.5×10^{-4} for band 2, 3.5×10^{-3} for band 3, and 3×10^{-3} for band 4 for the area considered below.

2.4. Block Diagram of the Algorithm

The block diagram of the proposed algorithm is shown in Figure 2. To estimate the ground surface reflectance, the following actions are performed:

1. Formation of the block of input data. Input data are the following: radiance received in the MODIS band $I_{r,ij}$ (i is the pixel line number, j is the pixel column number); aerosol optical depth (AOD) of the atmosphere; vertical profiles of temperature $T(z)$ and pressure $P(z)$; cloud mask n_{ij} ; information about the mutual positions of observed pixels, the sun, and the satellite (pixel coordinates $(\varphi_{N,ij}, \lambda_{N,ij})$, direction to the sun $(\theta_{sun,ij}, A_{sun,ij})$, direction to the satellite $(\theta_{d,ij}, A_{d,ij})$). These data can be borrowed from MODIS thematic products MOD021_L2, MOD03_L2, MOD07_L2, MOD35_L2, and MOD08_D3.
2. Construction of the atmospheric model. Satellite measurements of AOD, $T(z)$, and $P(z)$ formed the basis for constructing the atmospheric model. Profiles of the aerosol extinction and scattering coefficients are set based on MODTRAN models [39] closest in the aerosol optical depth to MODIS data. Profiles of the molecular scattering coefficients are set based on the temperature and pressure profiles and the values of the molecular scattering coefficients from [40]. Profiles of the molecular absorption coefficients are constructed based on the vertical temperature and pressure profiles, the MODTRAN model of the gas composition of the atmosphere for mid-latitude summer, and absorption cross-sections of atmospheric gases from the HITRAN database [41]. The atmospheric models can be found in the Supplementary Materials [37]. The algorithm for construction of these models is described in Appendix A.

3. Calculation of the areas S_{ij} . The image under consideration was divided into sections with respect to the closeness to the pixel centers. The algorithm for calculating the areas is described in the Supplementary Materials [37].
4. Calculation of the radiance $I_{atm,ij}$ for the radiation non-interacting with the ground surface.
5. Determination of the number l and angles of the boundaries θ_l of isoplanar zones (zones in which one PSF of the AE h can be used).
6. Calculation of direct transmittance at the “observed pixel–receiver” path τ_{ij} .
7. Calculation of the AE radii for isoplanar zones R_l .
8. Calculation of $h(\rho_w, \alpha_w, \mu_l)$ for each isoplanar zone and its integral over the entire ground surface $H(\mu_l)$.
9. Estimation of the number of pixels in an image (in image lines Nx_{ij} and columns Ny_{ij}) within the AE radius R_l for each pixel.
10. Solution of system of linear algebraic Equation (8) for luminosity of observed pixels Q_{ij} .
11. Calculation of ground surface irradiance neglecting the reflected radiation E_0 .
12. Calculation of the radii R_S of additional irradiance of the ground surface by surface pixels.
13. Calculation of $h_1(\rho_w)$ and its integral γ_1 .
14. Estimation of the number of pixels in an image (in image lines Mx_{ij} and columns My_{ij}) within the radius of additional irradiance formation R_S for each pixel.
15. Solution of system of nonlinear Equation (9) for surface reflectance $r_{surf,ij}$.

To implement this algorithm, we have developed eight Monte Carlo programs for determining the following parameters: S_{ij} , $I_{atm,ij}$, $k_1(\rho_w)$, $h(\theta_l, \rho_w, \alpha_w)$, $H(\theta_l)$, E_0 , $h_1(\rho_w)$, and γ_1 [27,38]. Let us touch briefly the approaches to simulation of these parameters. The radiance $I_{atm,ij}$ was simulated by the backward scheme with local estimates at collision point. The values of k_1 , H , and h were calculated by the Monte Carlo algorithm based on direct trajectories from the same point on the surface as a Lambertian source with the trajectory turned at each collision point so that the collision point is on the line of sight. This algorithm is described in detail in [42]. The value of E_0 was calculated by the Monte Carlo program with backward trajectories from the ground surface and local estimates at collision points. The value of h_1 and γ_1 were determined through direct Monte Carlo simulation. Most of the developed programs (except for the programs for k_1 , H , and h) were based on classical algorithms proposed in [43]. The Monte Carlo algorithms are considered in detail in Appendix B.

2.5. Algorithm Reliability

The reliability of results obtained with the developed Monte Carlo programs was checked in [27,38] through the comparison with the calculated data [44–48] and with analytical solutions in the single-scattering approximation. The performed comparisons allow us to state that, within the framework of the mentioned assumptions, the developed Monte Carlo programs provide reliable results.

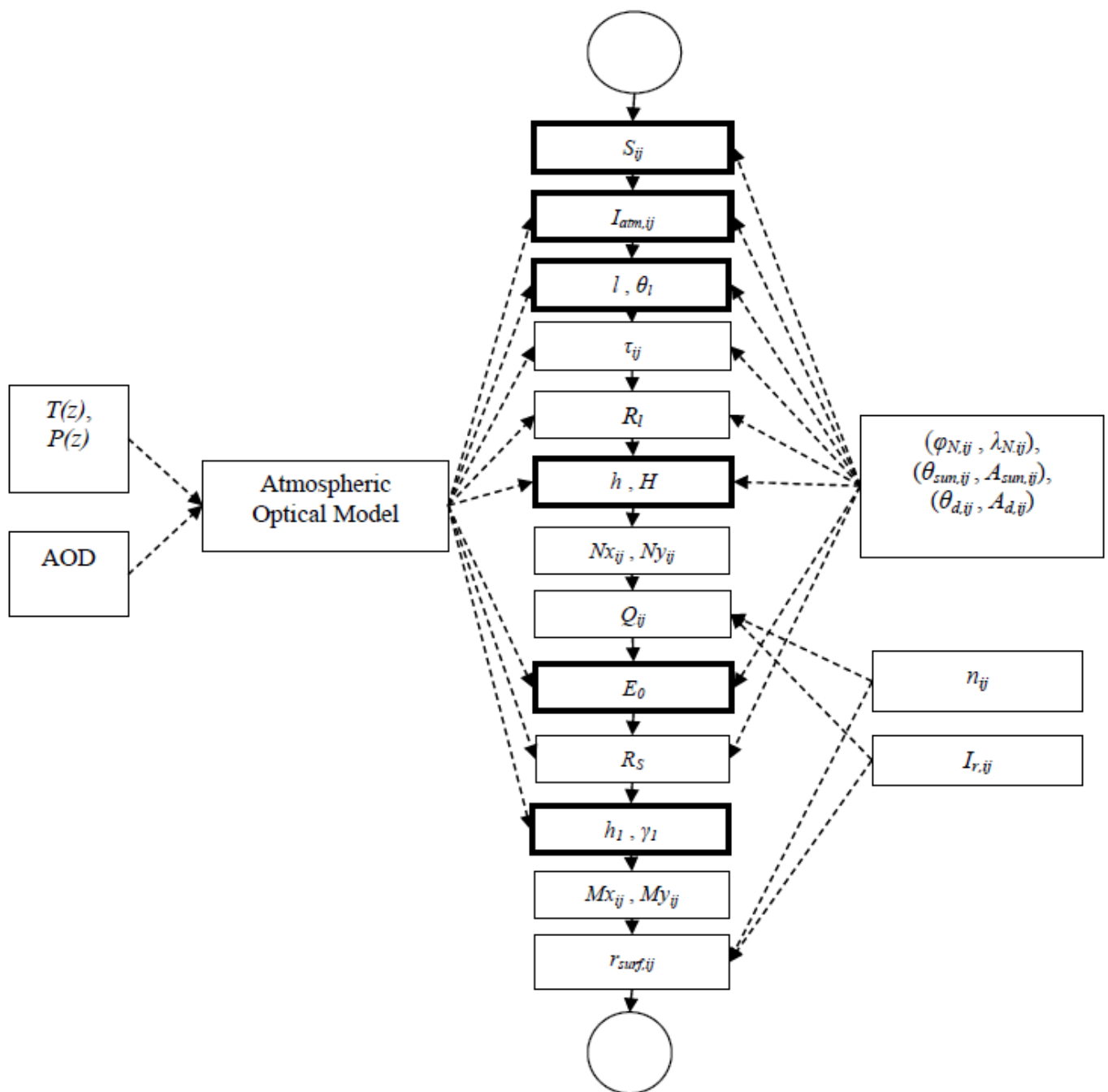


Figure 2. Block diagram of the algorithm for retrieval of surface reflectance. Units employing the Monte Carlo method are shown in black.

3. Algorithm Validation against Ground-Based Measurements

To assess the efficiency of the proposed algorithm, we have considered a test area with the coordinates 38.4–39.4°N, 8.25–9.25°W (Figure 3). For the site with the coordinates 38.829°N, 8.791°W (red dot in Figure 3) located at the center of this area, a series of ground-based measurements of surface reflectance was carried out in 2016 [28]. This is a Mediterranean grassland at Companhia das Lezirias, an estate of approximately 15,000 ha, located north-east of Lisbon, Portugal. Hyperspectral observations were performed using a FieldSpec3 spectroradiometer.

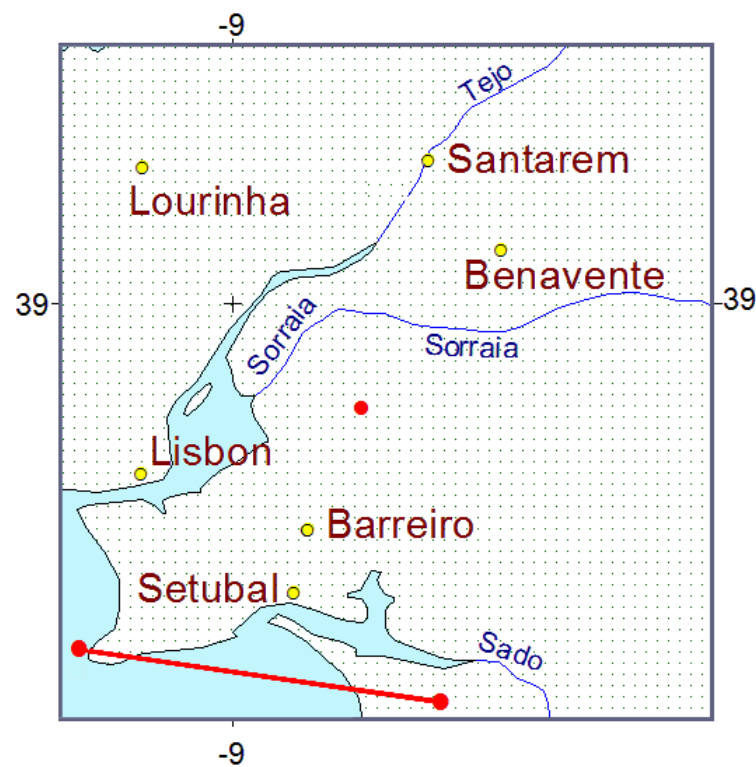


Figure 3. Test surface area with the coordinates 38.4–39.4°N, 8.25–9.25°W. The red dot is for the test site with the coordinates 38.829°N, 8.791°W, for which the results of ground-based measurements are reported in [28]. A red line is drawn from the pixel with coordinates 38.351°N, 8.660°W to the pixel with coordinates 38.438°N, 9.247°W

Measurements were taken at 24 closely spaced locations. The measured information can be an objective basis for validating the proposed algorithm. The test area is represented by grasslands. Thus, if the model results turn out to be close to the measured values of r_{surf} for this area, then we can say that the algorithm is applicable for retrieving the reflectance of territories covered with vegetation in the growing season. The algorithm was validated in the following way. Measurements for 1 April, 25 April, 25 May, and 3 June of 2016 are available in [28]. They are hyperspectral measurements with a step of 0.001 μm (Figure 4). These data were averaged over 24 sites and standard deviations were calculated. The data were averaged uniformly over wavelengths within the MODIS bands. The obtained averaged values and their standard deviation are given in Table 2.

For four MODIS bands of the TERRA and AQUA satellites (central wavelengths $\lambda = 0.645, 0.858, 0.469, \text{ and } 0.555 \mu\text{m}$) for the same dates and the pixels closest to the test area, the data of Table 2 were compared with the reflectances r_{surf} obtained by the proposed algorithm, the MOD09 algorithm, and the algorithm without atmospheric correction described by the following equation:

$$r_{surf, no\ cor, ij} = \frac{\pi I_{r, ij}}{S_{\lambda} \mu_{sun, ij}}, \quad (19)$$

where S_{λ} is the solar constant.

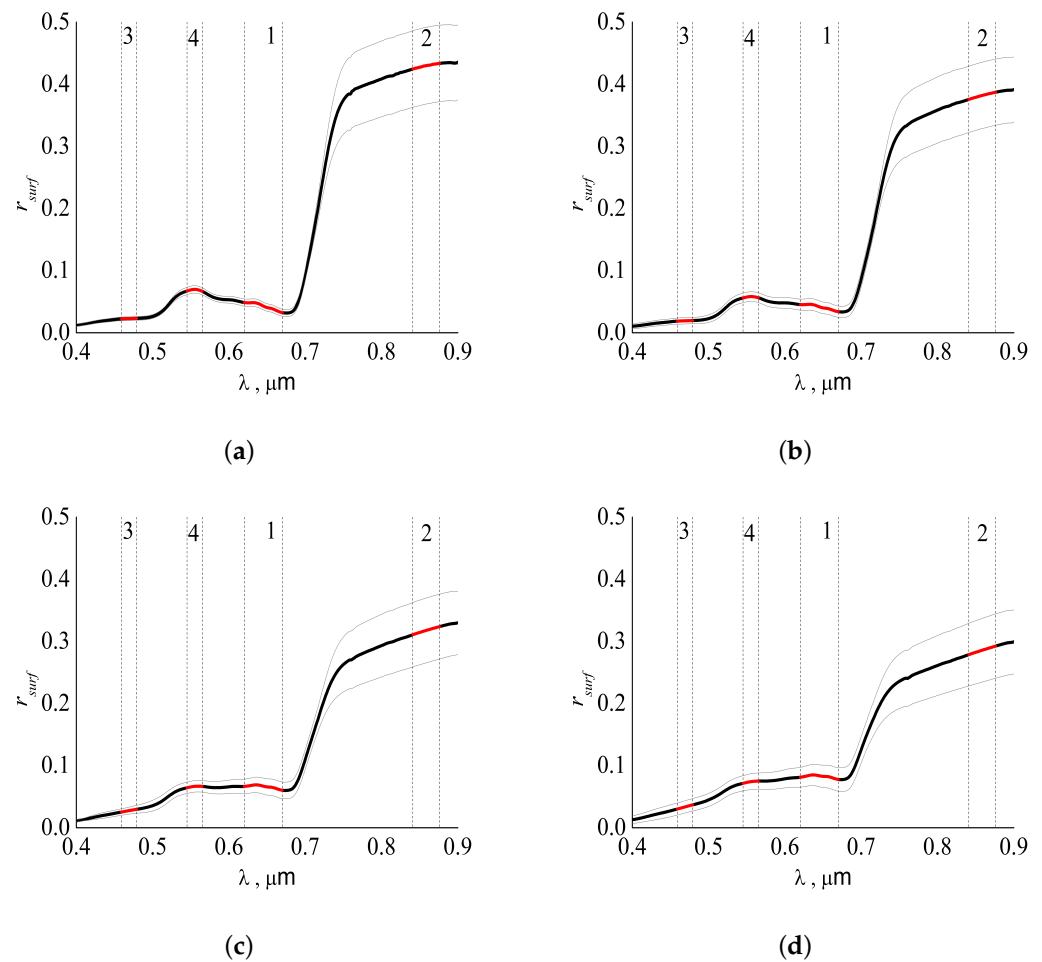


Figure 4. Ground-based measurements of reflectances of the surface area with coordinates 38.829°N, 8.791°W [28]: (a) 1 April 2016; (b) 25 April 2016; (c) 20 May 2016; (d) 3 June 2016. Numbers 1–4 are the numbers of the MODIS bands; thick lines are the average reflectances; thin lines are their standard deviations

Table 2. Ground-based measurements for average wavelengths of MODIS bands and their standard deviations (SD).

Date	MODIS Band							
	1		2		3		4	
	r_{surf}	SD	r_{surf}	SD	r_{surf}	SD	r_{surf}	SD
1 April 2016	0.0425	0.0060	0.4295	0.0616	0.0228	0.0030	0.0686	0.0059
25 April 2016	0.0414	0.0092	0.3818	0.0533	0.0192	0.0051	0.0573	0.0077
20 May 2016	0.0659	0.0128	0.3175	0.0521	0.0275	0.0057	0.0661	0.0092
3 June 2016	0.0823	0.0176	0.2857	0.0512	0.0336	0.0098	0.0737	0.0127

The comparison of the ground-based measurements with the results calculated by the three algorithms is performed in Figures 5 and 6 and Tables 3 and 4. The obtained values of surface reflectances can be found in the Supplementary Materials [37]. The results obtained by the proposed algorithm and by the MOD09 algorithm demonstrate a good agreement with the ground-based data except for the results of 1 April 2016 for band 2 of the both satellites. For bands 1, 3, and 4, the discrepancy ranges from -0.023 to 0.023 for the proposed algorithm and from -0.014 to 0.024 for MOD09. For band 2, for all the

considered days except for 1 April 2016, the discrepancy ranges from -0.064 to 0.067 for the proposed algorithm and from -0.059 to 0.044 for MOD09. The significant discrepancy for 1 April 2016 for band 2 is most likely reasoned by the difference between the used atmospheric models and the actual atmosphere. The comparison of the MOD09 results and the results of the proposed algorithm for the test site shows that they are in a good agreement for all the days for AQUA and for all the days except for 20 May 2016 for TERRA. The discrepancy for 20 May 2016 for the TERRA data is presumably due to differences in atmospheric models. For bands 1, 3, and 4, the results without atmospheric correction differ widely from the ground-based measurements, MOD09 results, and results provided by the proposed algorithm (the discrepancy from the ground-based measurements ranges from 0.012 to 0.154). As for band 2, for some days, the results without atmospheric correction are closer to the ground-based data than the MOD09 results and the results of our algorithm (for example, for the TERRA data for 20 May 2016). Thus, the proposed algorithm provides results no worse than the MOD09 algorithm for the test uniform area.

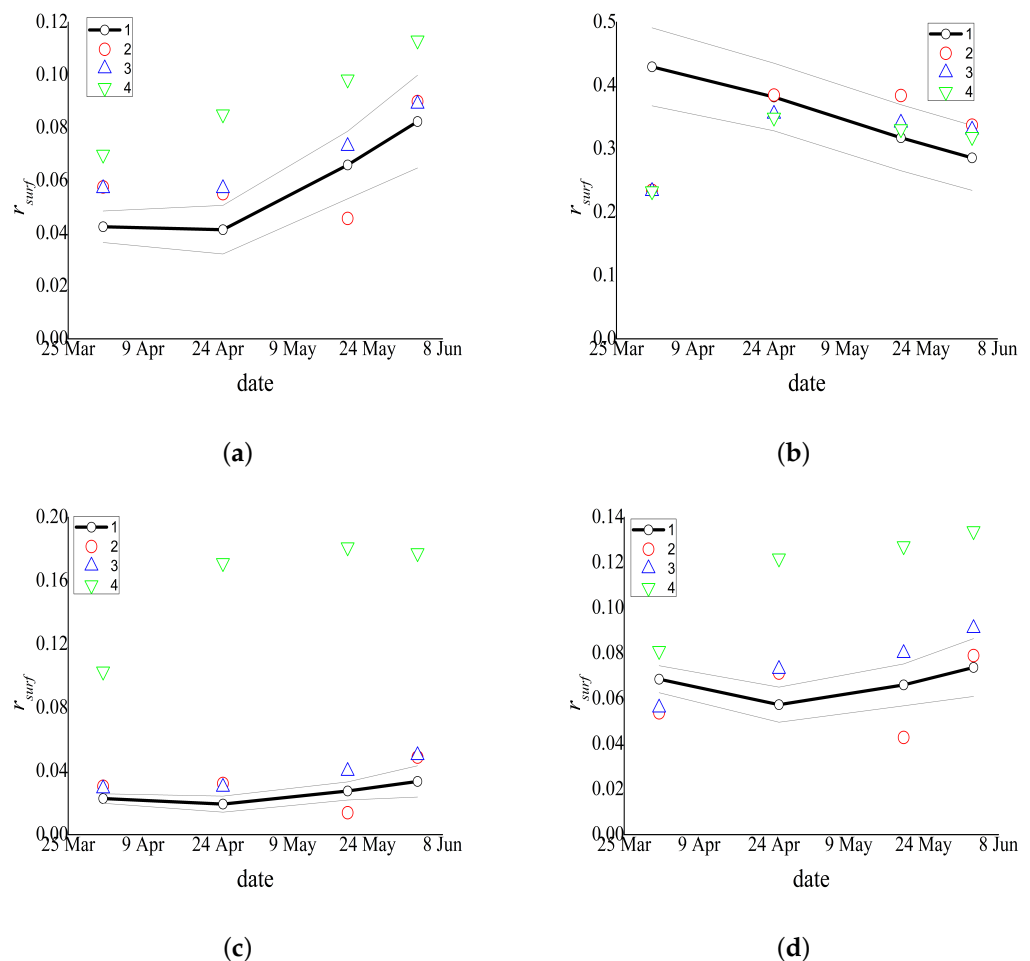


Figure 5. Comparison of averaged ground-based measurements [28] and the results provided by the three algorithms for the TERRA data: (1) averaged ground-based measurements and their standard deviations (gray), (2) proposed algorithm, (3) MOD09, (4) without atmospheric correction; MODIS band 1 ($\lambda = 0.62\text{--}0.67\ \mu\text{m}$) (a), 2 ($\lambda = 0.841\text{--}0.876\ \mu\text{m}$) (b), 3 ($\lambda = 0.459\text{--}0.479\ \mu\text{m}$) (c), and 4 ($\lambda = 0.545\text{--}0.565\ \mu\text{m}$) (d).

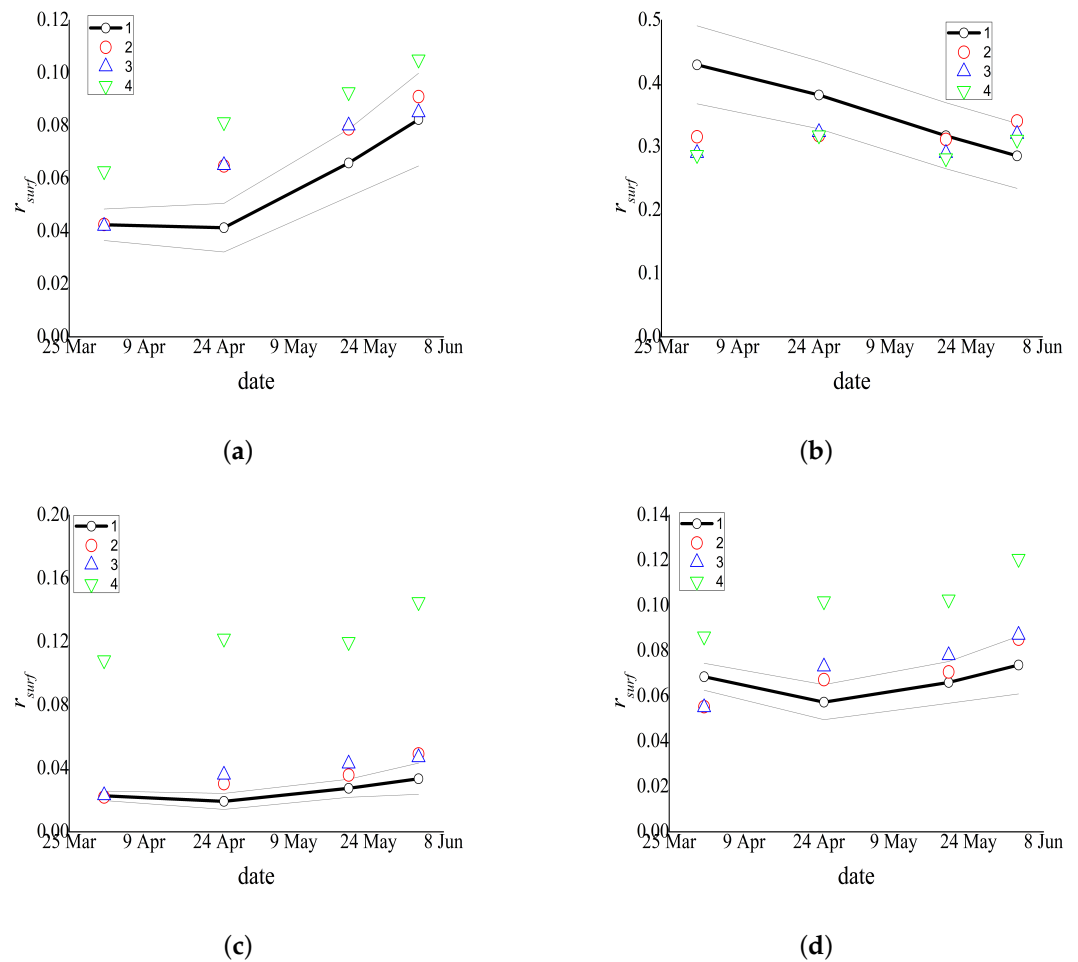


Figure 6. Comparison of averaged ground-based measurements [28] and the results provided by the three algorithms for the AQUA data: (1) averaged ground-based measurements and their standard deviations (gray), (2) proposed algorithm, (3) MOD09, (4) without atmospheric correction; MODIS band 1 ($\lambda = 0.62\text{--}0.67 \mu\text{m}$) (a), 2 ($\lambda = 0.841\text{--}0.876 \mu\text{m}$) (b), 3 ($\lambda = 0.459\text{--}0.479 \mu\text{m}$) (c), and 4 ($\lambda = 0.545\text{--}0.565 \mu\text{m}$) (d).

In addition, the results provided by the MOD09 algorithm, the proposed algorithm, and the algorithm without atmospheric correction were compared for the entire test area ($38.4\text{--}39.4^\circ\text{N}$, $8.25\text{--}9.25^\circ\text{W}$), four analyzed days, and four MODIS bands. The results of comparison are shown in Figures 7 and 8 and Table 5. Figures 9–11 exemplify the values of r_{surf} obtained by the three algorithms for 1 April 2016. The analysis shows that the results of the MOD09 and proposed algorithms correlate with the coefficient greater than 0.94. The results without atmospheric correction are also strongly correlated with MOD09: the correlation coefficient is greater than 0.73 for MODIS band 3 and 0.94 for all the other bands. The average discrepancy between the results of the proposed algorithm and MOD09 does not exceed 0.009 for bands 1, 3, and 4 and 0.017 for band 2. Based on the high correlation of the results provided by the algorithms, linear regressions were constructed (shown in Figures 7 and 8). The analysis of the regressions shows that, for nearly all the considered situations (except for TERRA band 4) for surfaces with the reflectance close to zero, the MOD09 values are, on average, higher than those of the proposed algorithm, but for the surface with high reflectance, the values given by the proposed algorithm are higher. This situation is likely due to the fact that the proposed algorithm better takes into account the effect that low-reflective surfaces seem more reflective due to the adjacency effect from highly reflective surfaces and vice versa. The analysis of the regression between MOD09 and the algorithm without correction shows that, for low-reflective surface, the algorithm

without atmospheric correction gives values higher than those of MOD09. This is primarily due to the fact that the algorithm without atmospheric correction ignores the influence of solar radiation non-interacting with the ground surface.

Table 3. Discrepancy of the averaged ground-based measurements [28] and the results provided by the three algorithms for the TERRA data.

MODIS Band	Date	Proposed Algorithm	MOD09 Algorithm	Algorithm without Atmospheric Correction
1	1 April 2016	0.015	0.015	0.027
1	25 April 2016	0.014	0.016	0.044
1	20 May 2016	−0.020	0.007	0.032
1	3 June 2016	0.008	0.007	0.031
2	1 April 2016	−0.195	−0.197	−0.196
2	25 April 2016	0.003	−0.027	−0.032
2	20 May 2016	0.067	0.024	0.014
2	3 June 2016	0.052	0.044	0.033
3	1 April 2016	0.008	0.006	0.080
3	25 April 2016	0.013	0.011	0.152
3	20 May 2016	−0.014	0.012	0.154
3	3 June 2016	0.015	0.016	0.144
4	1 April 2016	−0.015	−0.013	0.012
4	25 April 2016	0.014	0.016	0.065
4	20 May 2016	−0.023	0.014	0.061
4	3 June 2016	0.005	0.017	0.060

Table 4. Discrepancy of the averaged ground-based measurements [28] and the results provided by the three algorithms for the AQUA data.

MODIS Band	Date	Proposed Algorithm	MOD09 Algorithm	Algorithm without Atmospheric Correction
1	1 April 2016	9.00×10^{-5}	-4.80×10^{-4}	0.020
1	25 April 2016	0.023	0.024	0.040
1	20 May 2016	0.013	0.014	0.027
1	3 June 2016	0.009	0.003	0.023
2	1 April 2016	−0.114	−0.140	−0.142
2	25 April 2016	−0.064	−0.059	−0.064
2	20 May 2016	−0.006	−0.028	−0.035
2	3 June 2016	0.055	0.034	0.026
3	1 April 2016	−0.001	2.20×10^{-4}	0.086
3	25 April 2016	0.011	0.017	0.103
3	20 May 2016	0.008	0.015	0.092
3	3 June 2016	0.016	0.013	0.112
4	1 April 2016	−0.013	−0.014	0.018
4	25 April 2016	0.010	0.016	0.045
4	20 May 2016	0.005	0.012	0.037
4	3 June 2016	0.011	0.013	0.047

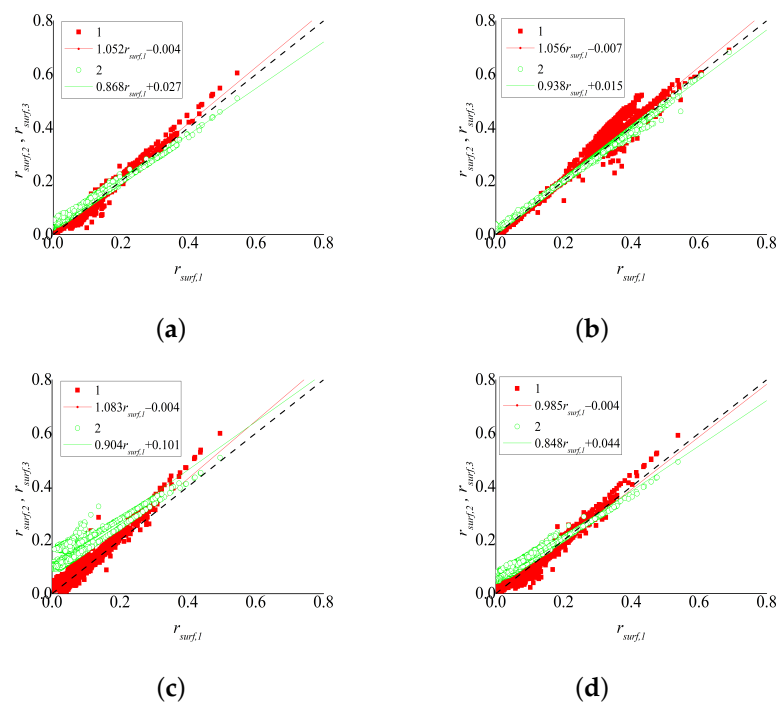


Figure 7. Comparison of reflectances provided by MOD09 (plotted along the Ox axis), the proposed algorithm (symbols 1), and the algorithm without atmospheric correction (symbols 2) (plotted along the Oy axis) for TERRA; MODIS band 1 ($\lambda = 0.62\text{--}0.67\ \mu\text{m}$) (a), 2 ($\lambda = 0.841\text{--}0.876\ \mu\text{m}$) (b), 3 ($\lambda = 0.459\text{--}0.479\ \mu\text{m}$) (c), and 4 ($\lambda = 0.545\text{--}0.565\ \mu\text{m}$) (d).

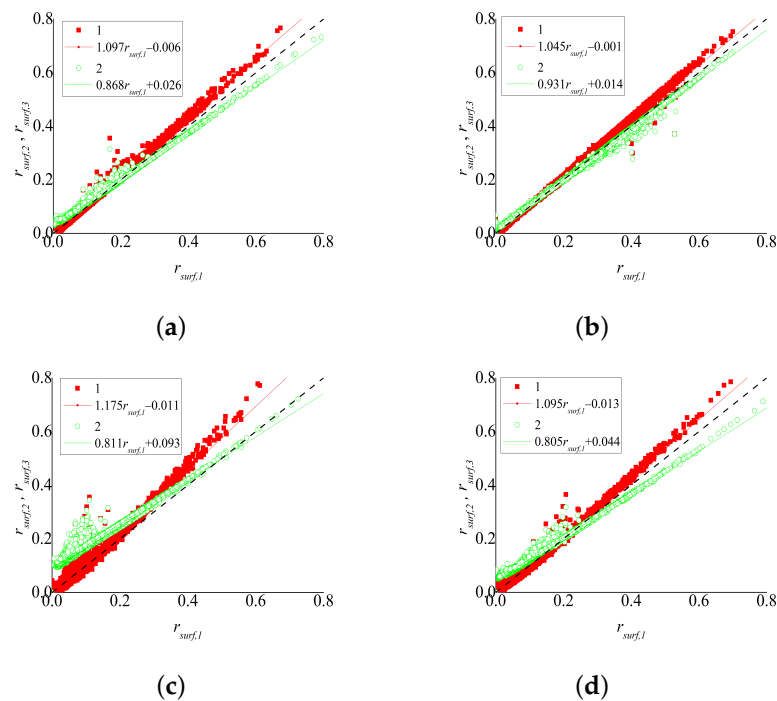


Figure 8. Comparison of reflectances provided by MOD09 (plotted along the Ox axis), the proposed algorithm (symbols 1), and the algorithm without atmospheric correction (symbols 2) (plotted along the Oy axis) for AQUA; MODIS band 1 ($\lambda = 0.62\text{--}0.67\ \mu\text{m}$) (a), 2 ($\lambda = 0.841\text{--}0.876\ \mu\text{m}$) (b), 3 ($\lambda = 0.459\text{--}0.479\ \mu\text{m}$) (c), and 4 ($\lambda = 0.545\text{--}0.565\ \mu\text{m}$) (d).

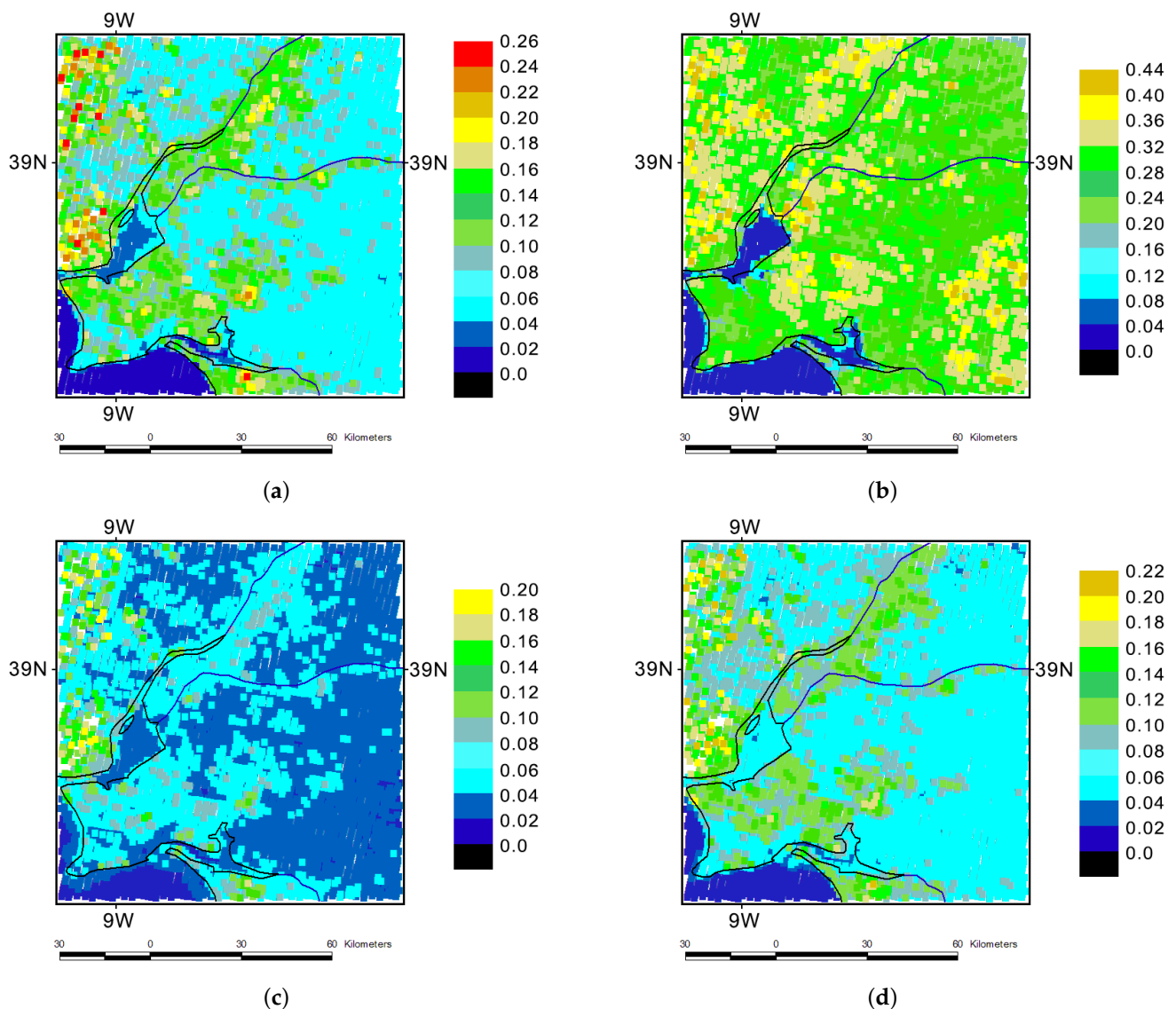


Figure 9. Example of reflectances calculated by the proposed algorithm for four MODIS bands (TERRA, 1 April 2016). The values below 0 correspond to negative reflectance. MODIS band 1 ($\lambda = 0.62\text{--}0.67\ \mu\text{m}$) (a), 2 ($\lambda = 0.841\text{--}0.876\ \mu\text{m}$) (b), 3 ($\lambda = 0.459\text{--}0.479\ \mu\text{m}$) (c), and 4 ($\lambda = 0.545\text{--}0.565\ \mu\text{m}$) (d).

In the southwestern part of the test area, where some territories are covered with water, the MOD09 algorithm often gives negative values of reflectance for the considered days. For example, for 1 April 2016 for the TERRA data, it yields negative reflectance for 4.8% of cloudless pixels in band 1, 5.9% in band 2, 3.8% in band 3, and 2.7% in band 4. At the same time, the proposed algorithm gives significantly fewer negative values for water areas (for example, for the same day for the TERRA data, 2.1% negative reflectance values for band 1 and 0% for the other bands). As an example, Figure 12 shows the values of r_{surf} for one of the image lines from the pixel with coordinates 38.351°N , 8.660°W to the pixel with coordinates 38.438°N , 9.247°W (red line in Figure 3) as provided by the three analyzed algorithms. It can be seen that the MOD09 algorithm gives zero and negative reflectances for the most pixels in fragments with low reflectance. The proposed algorithm gives much fewer negative results (Figure 12a) or only positive results (Figure 12b–d). For the situation under consideration, the MOD09 atmospheric model and the one we used differed. However, test comparisons for a uniform area (Tables 3 and 4) allow us to state that the main reason for the differences is how the algorithm we propose takes into account

the adjacency effect and additional illumination by reflected radiation. Thus, the advantage of the proposed algorithm in comparison with MOD09 manifests itself in surface areas with a significant change in reflectance.

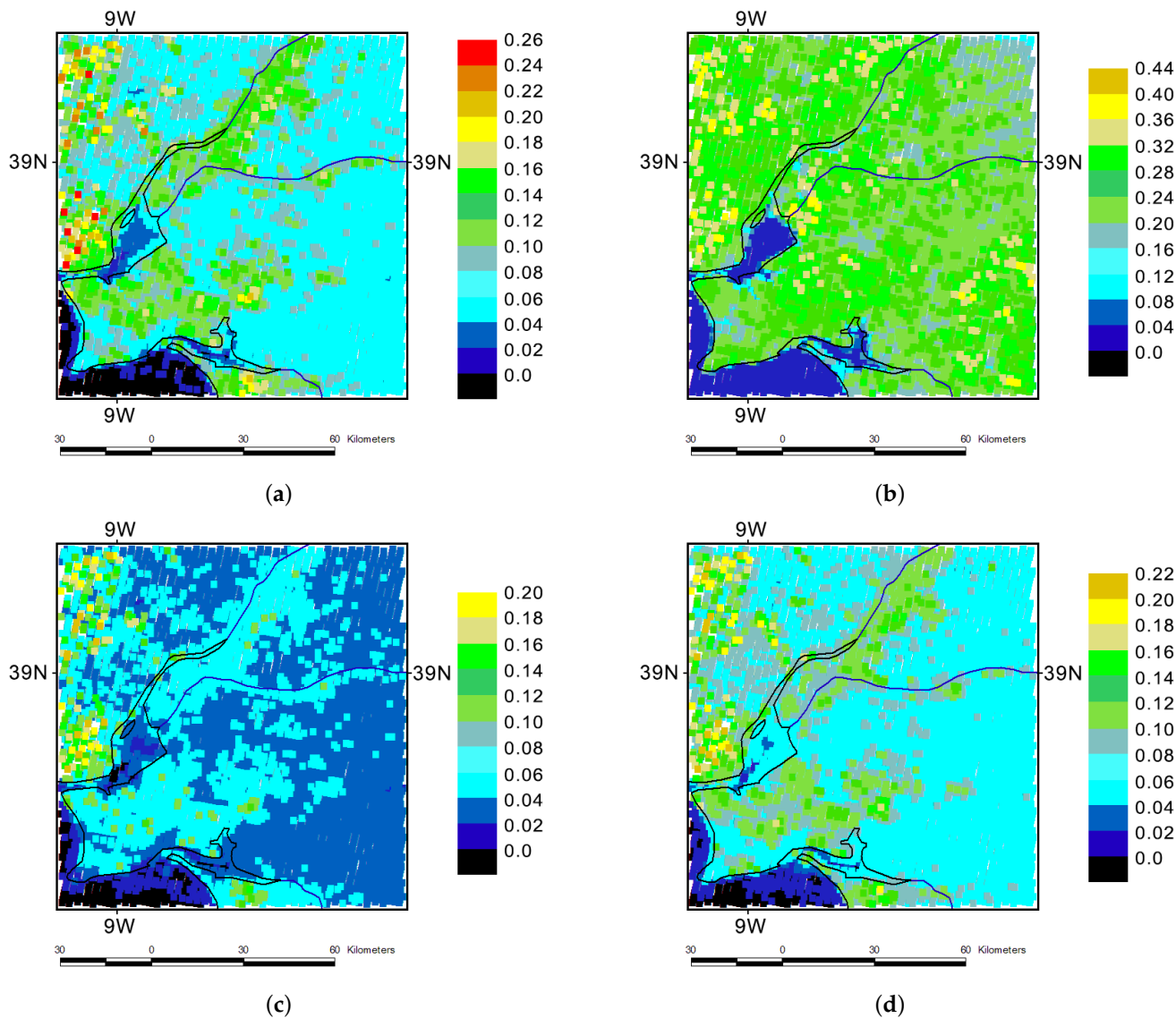


Figure 10. Example of reflectances calculated by the MOD09 algorithm for four MODIS bands (TERRA, 1 April 2016). The values below 0 correspond to negative reflectance. MODIS band 1 ($\lambda = 0.62\text{--}0.67 \mu\text{m}$) (a), 2 ($\lambda = 0.841\text{--}0.876 \mu\text{m}$) (b), 3 ($\lambda = 0.459\text{--}0.479 \mu\text{m}$) (c), and 4 ($\lambda = 0.545\text{--}0.565 \mu\text{m}$) (d).

Table 5. Pearson correlation r , average discrepancies $|\overline{\Delta r_{surf}}|$, and standard deviations (SD) of MOD09 results (1) from the results of the proposed algorithm (2) and algorithm without atmospheric correction (3) for the considered AQUA and TERRA data.

MODIS Band	No Correction			Proposed Algorithm		
	r	SD	$\overline{\Delta r_{surf}}$	r	SD	$\overline{\Delta r_{surf}}$
AQUA						
1	0.997	0.008	0.014	0.997	0.007	0.006
2	0.999	0.006	0.009	0.994	0.009	0.017
3	0.975	0.014	0.081	0.987	0.012	0.009
4	0.993	0.009	0.025	0.994	0.007	0.007

Table 5. Cont.

MODIS Band	No Correction			Proposed Algorithm		
	r	SD	$\overline{\Delta r_{surf}}$	r	SD	$\overline{\Delta r_{surf}}$
TERRA						
1	0.986	0.010	0.010	0.984	0.006	0.004
2	0.999	0.005	0.003	0.985	0.015	0.007
3	0.734	0.052	0.060	0.948	0.009	0.005
4	0.948	0.018	0.020	0.963	0.008	0.006

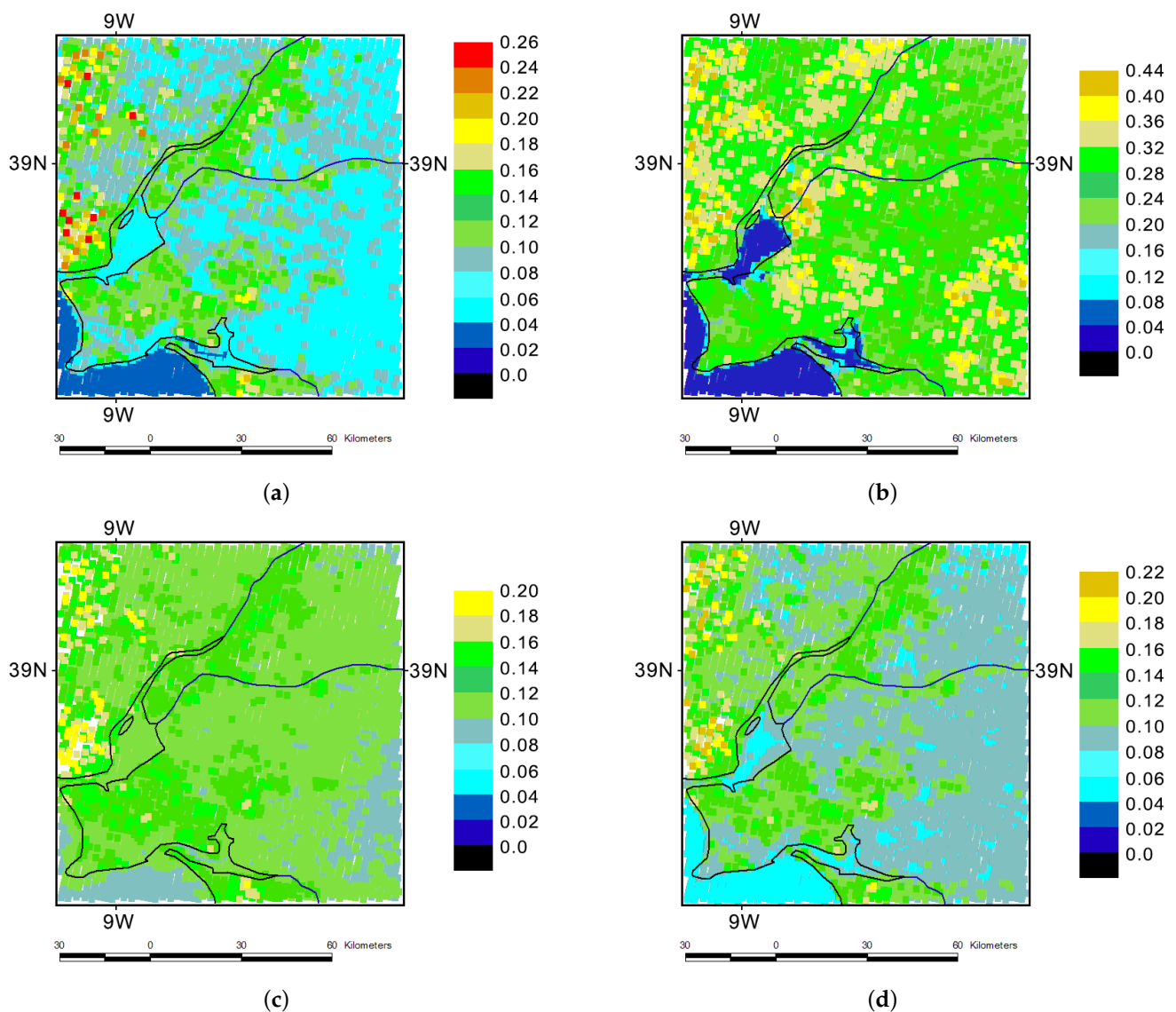


Figure 11. Example of reflectances calculated by the algorithm without atmospheric correction for four MODIS bands (TERRA, 1 April 2016). MODIS band 1 ($\lambda = 0.62\text{--}0.67 \mu\text{m}$) (a), 2 ($\lambda = 0.841\text{--}0.876 \mu\text{m}$) (b), 3 ($\lambda = 0.459\text{--}0.479 \mu\text{m}$) (c), and 4 ($\lambda = 0.545\text{--}0.565 \mu\text{m}$) (d).

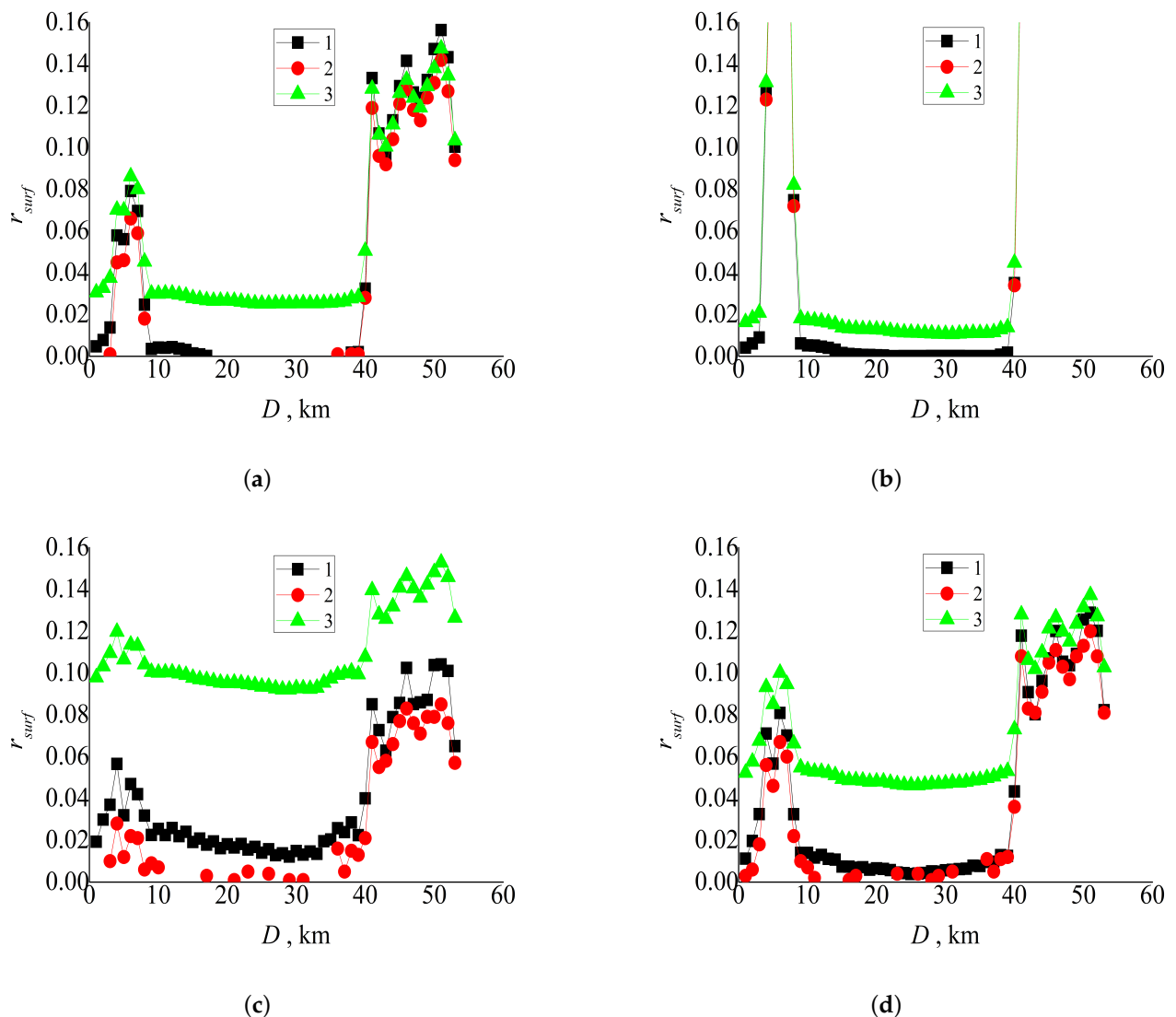


Figure 12. Values of reflectance obtained by the three algorithms for line 879 of the TERRA image of the test area for 1 April 2016 from the pixel with coordinates 38.351°N , 8.660°W to the pixel with coordinates 38.438°N , 9.247°W . Negative values of r_{surf} are omitted. The distance to the pixel with coordinates 38.351°N , 8.660°W is plotted along the Ox axis: (1) proposed algorithm; (2) MOD09 algorithm; (3) without atmospheric correction; MODIS band 1 ($\lambda = 0.62\text{--}0.67\ \mu\text{m}$) (a), 2 ($\lambda = 0.841\text{--}0.876\ \mu\text{m}$) (b), 3 ($\lambda = 0.459\text{--}0.479\ \mu\text{m}$) (c), and 4 ($\lambda = 0.545\text{--}0.565\ \mu\text{m}$) (d).

4. Conclusions

Following our analysis, the following most important results have been obtained:

(1) Comparison of the results provided by the proposed algorithm and the MOD09 algorithm based on TERRA and AQUA data with ground-based measurements for the area with coordinates 38.829°N , 8.791°W demonstrates a good agreement.

(2) For bands 1, 3, and 4, the discrepancy between the calculated results and the ground-based measurements [28] ranges from -0.023 to 0.023 for the proposed algorithm and from -0.014 to 0.024 for MOD09. For band 2, for all the analyzed days except for 1 April 2016, the discrepancy ranges from -0.064 to 0.067 for the proposed algorithm and from -0.059 to 0.044 for MOD09.

(3) The comparison of the results provided by the MOD09 algorithm and the proposed algorithm for the area with coordinates $38.4\text{--}39.4^{\circ}\text{N}$, $8.25\text{--}9.25^{\circ}\text{W}$ for all the four analyzed days and four MODIS bands shows that they correlate with the coefficient higher than 0.94.

The average discrepancy between the results for the both algorithms does not exceed 0.009 for bands 1, 3, and 4 and 0.017 for band 2.

(4) An analysis of the regressions between the results of MOD09 and the proposed algorithm shows that the values of MOD09 are, on average, higher than those of the proposed algorithm for surfaces with reflectance close to zero, but the values obtained by the proposed algorithm are higher for surfaces with high reflectance.

(5) For fragments with low reflectance (water surfaces), MOD09 algorithm often gives zero or negative reflectance values for the considered pixels. At the same time, the proposed algorithm gives either much fewer negative results (Figure 12a) or only positive values (Figure 12b–d).

The use of the criterion of separation of isoplanar zones in the proposed algorithm and similar algorithms allows one to set the error level and to calculate the needed number of PSFs for a given image, a receiver band, and observation conditions by Equation (10). Criteria (13) and (15) for estimating the radii of the adjacency effect and formation of additional irradiance of the ground surface allow obtaining the upper estimate of the size of zones, outside of which these effects are small. The proposed criteria are suitable for use in all alternative algorithms that take into account the adjacency effect and the influence of the inhomogeneity of surface reflection in formation of surface illumination. Interpolation Equations (16)–(18) for the radiation non-interacting with the surface can also be used in similar algorithms.

The comparison with the ground-based measurements and MOD09 data for TERRA and AQUA satellite data shows that, for the uniform surface area, the proposed algorithm gives results no worse than MOD09: in some days, our results are closer to the average ground-based measurements, while, in others, the MOD09 results are closer. The test area was chosen because the data of ground-based measurements are available for it [28]. The proposed algorithm can be used for other surface areas as well. In the future, we plan to expand significantly the set of ground-based data, for which the algorithm was validated, to such data as RadCalNet [49].

The employed atmospheric model uses data on the aerosol optical depth and temperature and pressure profiles as input data. Obtaining these data is a separate problem. The algorithm allows using other atmospheric models. Its operation requires profiles of the aerosol and molecular extinction and scattering coefficients, as well as aerosol scattering phase function, which can be obtained by various methods.

The adjacency effect is even more important for medium and high spatial resolution images than for low resolution images. The MODIS data were chosen for the comparison due to the high capabilities of the MOD09 algorithm, which allows better testing of the proposed algorithm. The proposed method can be readily adapted to use with other satellite devices having bands in the visible and NIR ranges. In the future, the applicability of the proposed algorithm will be extended to satellites of medium and high spatial resolution, such as Landsat and Russian Kanopus-V and Meteor-M satellites. Currently, the method cannot be used in batch mode yet. In the current version, the processing of a 5-minute MODIS image takes about 2 h of PC time (16 × AMD Ryzen 7 1800X Eight-Core Processor). In the nearest future, it is planned to adapt the software package for cluster operation in batch mode.

Factors such as the non-Lambertian character of reflection and the surface topography remain beyond the scope of this study. In the further studies, we plan to take into account the non-Lambertian reflection in the same way as in [29]. The surface topography is an important factor only for surfaces with significant height difference. It can be included in consideration by adding factors taking into account that a part of the solid angle can be overlapped by surfaces of adjacent fragments in Equations (8) and (9).

In general, the proposed algorithm contributes significantly to the solution of some problems arising when considering the adjacency effect and additional surface illumination, and it can be used for a wide range of atmospheric correction problems.

Author Contributions: Conceptualization, M.V.T. and V.V.B.; methodology, M.V.T. and V.V.B.; software, M.V.T., M.V.E., A.V.Z., M.N.Z. and A.S.B.; validation, M.V.T., A.V.Z. and M.V.E.; investigation, M.V.T., M.V.E. and A.S.B.; resources, M.V.E. and M.V.T.; writing—original draft preparation, M.V.T. All authors have read and agreed to the published version of the manuscript.

Funding: The study was carried out within the framework of the State Task for the Institute of Atmospheric Optics SB RAS.

Institutional Review Board Statement: Not applicable.

Informed Consent Statement: Not applicable.

Data Availability Statement: https://github.com/MarinaEngel/Atmosphere_2023 (accessed on 31 January 2023)

Acknowledgments: We are thankful to the authors of [28] for the ground-based measurements of reflectance that have allowed us to validate our algorithm. We are also thankful to the NASA team for the possibility of using MODIS thematic products.

Conflicts of Interest: The authors declare no conflicts of interest.

Appendix A. Description of Atmospheric Models

The atmospheric models used in the algorithm are based on the MODTRAN mid-latitude summer models [39]. The atmospheric models comprised the aerosol and molecular scattering and extinction coefficients, as well as the aerosol scattering phase functions for 32 vertically homogeneous layers, whose boundaries are given in the MODTRAN models [39]. The molecular scattering phase function was taken in the form

$$g_m(\cos\gamma) = \frac{3}{8}(1 + \cos^2\gamma) \quad (\text{A1})$$

where γ is the scattering angle. The aerosol scattering phase function was specified tabularly for each i -th layer and 34 cosines of scattering angles $\mu_{\gamma,j} \equiv \cos\gamma_j : (\mu_{\gamma,j}, g_{a,i}(\mu_{\gamma,j}))$ according to the MODTRAN atmospheric models. The aerosol scattering and extinction coefficients for each layer were taken from the MODTRAN model closest in the aerosol optical depth to the MODIS satellite data. The molecular scattering coefficients for 32 layers were determined as

$$\sigma_{sm,i} = \sigma_{sm,0} \frac{P_i}{P_0} \frac{T_0}{T_i} \quad (\text{A2})$$

where $\sigma_{sm,0}$ is the molecular scattering coefficient at $T_0 = 273.1$ K, $P_0 = 1013$ mbar for the considered MODIS band [40]; T_i is the air temperature in the i -th atmospheric layer, and P_i is the atmospheric pressure in the i -th atmospheric layer. The T_i and P_i profiles were taken from the MODIS satellite data. The profiles of molecular absorption coefficients $\sigma_{am,i}$ for the considered MODIS bands were calculated from the molecular absorption cross sections of O_3 , O_2 , and H_2O that are available from the HITRAN database [41] with a step of 0.1 cm^{-1} , as well as the T_i and P_i profiles and the profiles of number densities $N_{k,i}$ of atmospheric gases from the MODTRAN model. The calculation was carried out by the following equations:

$$\sigma_{am,i} = \sum_{k=1}^3 \chi_k(P_i, T_i) N_{k,i} \quad (\text{A3})$$

$$\chi_k = \frac{1}{\lambda_{max} - \lambda_{min}} \int_{\lambda_{min}}^{\lambda_{max}} f_k(P_i, T_i, \lambda) d\lambda \quad (\text{A4})$$

where $N_{k,i}$ is the number density of the k -th molecule in the i -th layer, in mol/cm^3 ; χ_k is the absorption cross section of the k -th gas averaged over the considered MODIS band, in cm^2/mol ; λ_{min} , λ_{max} are boundaries of a MODIS band, in μm ; $f_k(P_i, T_i, \lambda)$ is the absorption cross section of the k -th gas in the i -th atmospheric layer in a 0.1 cm^{-1} wide wavelength

range centered at a wavelength λ at the temperature T_i and atmospheric pressure P_i , in cm^2/mol .

The vertical absorption optical depth for MODIS bands 1–4 for the considered situations was from 0.8 to 20% of the total vertical optical depth. Therefore, the monochromatic approximation can be used.

Appendix B. Monte Carlo Algorithms

In this study, we use eight Monte Carlo programs to simulate the following parameters: S_{ij} , $I_{atm,ij}$, h , k_1 , H , E_0 , h_1 , and γ_1 . The calculations for $I_{atm,ij}$, h , k_1 , H , E_0 , h_1 , and γ_1 are performed for the given atmospheric model (Appendix A), and the same classical algorithm is used for simulation of photon histories in a medium [43]. We first consider the stages of this algorithm that are common to all the parameters and then the stages that distinguish the programs from each other. Photon histories are simulated in the following way [43]:

1. The following initial “photon” parameters are set: the initial photon position described by the Cartesian coordinates (x_0, y_0, z_0) , the direction of the trajectory described by the direction cosines (a_0, b_0, c_0) , and the initial photon weight w_0 . The initial data for each of the programs are defined differently.

2. The random optical depth of the photon free path is determined as

$$\tau_n = -\ln \alpha_1 \quad (\text{A5})$$

where α_1 is a random value distributed uniformly in the range $[0,1]$.

3. The coordinate of the next photon collision with the medium is determined as

$$x_n = x_{n-1} + a_{n-1}l_n \quad (\text{A6})$$

$$y_n = y_{n-1} + b_{n-1}l_n \quad (\text{A7})$$

$$z_n = z_{n-1} + c_{n-1}l_n \quad (\text{A8})$$

where l_n is the photon free path length determined from the random optical depth of the photon free path; $(x_{n-1}, y_{n-1}, z_{n-1})$ are coordinates of the previous collision of the photon trajectory with the medium; $(a_{n-1}, b_{n-1}, c_{n-1})$ is the direction of the photon trajectory.

4. It is determined whether the photon trajectory intersects the boundary of the medium. If no, then the algorithm proceeds to step 5. If yes, then the algorithm returns to step 1 (the next trajectory is simulated).

5. If the collision point falls within the medium, then, depending on the parameter to be determined, either local estimation or direct transition to step 6 is performed.

6. The type of photon interaction with the medium is determined as

$$\begin{cases} 0 \leq \alpha_2 \leq \frac{\sigma_{ta,n}}{\sigma_{ta,n} + \sigma_{tm,n}}, \text{ aerosol} \\ \frac{\sigma_{ta,n}}{\sigma_{ta,n} + \sigma_{tm,n}} < \alpha_2 \leq 1, \text{ molecular} \end{cases} \quad (\text{A9})$$

where α_2 is a random value distributed uniformly in the range $[0,1]$; $\sigma_{ta,n}$, $\sigma_{tm,n}$ are the aerosol and molecular extinction coefficients at the n -th collision point, respectively.

7. The photon weight decreases by the energy absorbed as a result of the interaction

$$w_n = w_{n-1} \frac{\sigma_{s,n}}{\sigma_{t,n}} \quad (\text{A10})$$

where $\sigma_{s,n}$, $\sigma_{t,n}$ are the scattering and extinction coefficients at the n -th collision point for the corresponding type of interaction (molecular or aerosol), respectively; w_{n-1} is the photon weight at the previous collision.

8. A random cosine of the scattering angle is selected. The following set of actions is performed:

(A) A random number of the node j , within which the scattering occurred, is determined:

$$j : \alpha_3 \leq G_n(\mu_{\gamma,j}) \equiv \int_{\mu_{\gamma,j}}^1 g_n(\mu) d\mu \tag{A11}$$

where α_3 is a random value distributed uniformly in the range $[0,1]$; g_n is the scattering phase function for the n -th collision point; $\mu_{\gamma,j}$ are cosines of the scattering angles, for which the scattering phase function is set.

(B) A random cosine of the scattering angle μ is determined

$$\mu = \mu_{\gamma,j} + \frac{\alpha_3 - G_n(\mu_{\gamma,j})}{G_n(\mu_{j-1}) - G_n(\mu_{\gamma,j})} (\mu_{\gamma,j-1} - \mu_{\gamma,j}) \tag{A12}$$

(C) A random azimuthal scattering angle is determined

$$\varphi = 2\pi\alpha_4 \tag{A13}$$

where α_4 is a random value distributed uniformly in the range $[0,1]$.

9. A new wandering direction is determined as

$$\begin{cases} a_n = a_{n-1} \mu - (b_{n-1} \sin \varphi + a_{n-1} c_{n-1} \cos \varphi) \sqrt{\frac{1 - \mu^2}{1 - (c_{n-1})^2}} \\ b_n = b_{n-1} \mu - (a_{n-1} \sin \varphi - b_{n-1} c_{n-1} \cos \varphi) \sqrt{\frac{1 - \mu^2}{1 - (c_{n-1})^2}} \\ c_n = c_{n-1} \mu + (1 - (c_{n-1})^2) \sqrt{\frac{1 - \mu^2}{1 - (c_{n-1})^2}} \end{cases} \tag{A14}$$

where $(a_{n-1}, b_{n-1}, c_{n-1})$ are the direction cosines of the trajectory direction before scattering; (a_n, b_n, c_n) are the direction cosines of the trajectory direction after scattering.

10. Transition to step 2.

Next, we consider the differences in the simulation of parameters.

(A) Simulation of I_{atm} . The simulation is carried out by the backward scheme with local estimates at the collision points. The initial conditions are set as follows:

$$(x_0, y_0, z_0) = (x_{sat}, y_{sat}, z_{sat}), \tag{A15}$$

$$(a_0, b_0, c_0) = (a_{sat}, b_{sat}, c_{sat}), \tag{A16}$$

$$w_0 = 1 \tag{A17}$$

where $(x_{sat}, y_{sat}, z_{sat})$ are the Cartesian coordinates of the satellite; $(a_{sat}, b_{sat}, c_{sat})$ is the direction of the optical axis of the satellite.

At step 5 of the simulation of photon trajectories, the local estimation of the following form is performed:

$$I_n = w_n \frac{\sigma_{sa,n} g_{a,n}(\mu_n) + \sigma_{sm,n} g_{m,n}(\mu_n)}{2\pi(\sigma_{ta,n} + \sigma_{tm,n})} \exp(-\tau_n) \tag{A18}$$

$$\mu_n = b_{n-1} \sqrt{1 - \mu_{sun}^2} + c_{n-1} \mu_{sun} \tag{A19}$$

where $\sigma_{sa,n}, \sigma_{sm,n}$ are the aerosol and molecular scattering coefficients at the n -th collision point, respectively; $g_{a,n}, g_{m,n}$ are the aerosol and molecular scattering phase functions at the n -th collision point, respectively; μ_{sun} is the cosine of the solar zenith angle; and τ_n is the optical depth from the collision point (x_n, y_n, z_n) to the atmospheric top in the direction to the sun.

(B) Simulation of E_0 . The simulation is carried out by the backward scheme with local estimates at the collision points. The initial conditions are set as follows:

$$(x_0, y_0, z_0) = (0, 0, R_e) \quad (\text{A20})$$

$$(a_0, b_0, c_0) = (\sin \varphi_0 \sqrt{1 - \mu_0^2}, \cos \varphi_0 \sqrt{1 - \mu_0^2}, \mu_0) \quad (\text{A21})$$

$$\mu_0 = \sqrt{\alpha_5} \quad (\text{A22})$$

$$\varphi_0 = 2\pi \alpha_6 \quad (\text{A23})$$

$$w_0 = \pi \quad (\text{A24})$$

where α_5, α_6 are random values distributed uniformly in the range [0,1].

The local estimation is performed by Equation (A18).

(C) Simulation of γ_1 and h_1 . The simulation is carried out by the direct scheme. The initial conditions are set as follows:

$$(x_0, y_0, z_0) = (0, 0, R_e) \quad (\text{A25})$$

$$(a_0, b_0, c_0) = (\sin \varphi_0 \sqrt{1 - \mu_0^2}, \cos \varphi_0 \sqrt{1 - \mu_0^2}, \mu_0) \quad (\text{A26})$$

$$w_0 = 1 \quad (\text{A27})$$

$$\mu_0 = \sqrt{\alpha_7} \quad (\text{A28})$$

$$\varphi_0 = 2\pi \alpha_8 \quad (\text{A29})$$

where α_7, α_8 are random values distributed uniformly in the range [0,1].

Steps 1–10 of photon history modeling are performed. At step 4, if the photon trajectory intersects the atmospheric bottom, then the photon weights w_n are summed up over the trajectories. In the case of h_1 simulation, the ground surface is divided into rings with the surface radii ρ_w from the point $(0, 0, R_e)$, and the summation is performed separately for each cell. The parameters γ_1 and h_1 are simulated separately, since obtaining a statistically reliable estimate for γ_1 requires approximately three orders of magnitude less trajectories.

(D) Simulation of k_1, h , and H . These parameters are simulated in a similar way. The simulation is carried out by the direct scheme with local estimates at the collision points. The initial conditions are set by Equations (A25)–(A29). At step 5, for each collision point, the coordinates at the current and previous collision points are recorded. The collision point and the previous collision point are rotated around the center of the Earth so that the collision point to be on the line of sight of the satellite system. The algorithm of rotation is described in detail in [42]. After the rotation, the radiation coming from the collision point to the satellite system is estimated. The previous collision point is needed to find the direction of the trajectory at the collision point after the rotation. When calculating H , the radiance is gathered throughout the Earth's surface. In calculation of k_1 , the spherical earth's surface is divided into rings, and to calculate h , the rings are additionally divided uniformly along the azimuth.

References

1. Otterman, J.; Fraser, R.S. Adjacency effects on imaging by surface reflection and atmospheric scattering: Cross radiance to zenith. *Appl. Opt.* **1979**, *18*, 2852–2860. [\[CrossRef\]](#)
2. Vanhellemont, Q.; Ruddick, K. Turbid wakes associated with offshore wind turbines observed with Landsat 8. *Remote Sens. Environ.* **2014**, *145*, 105–115. [\[CrossRef\]](#)
3. Cox, C.; Munk, W. Measurement of the Roughness of the Sea Surface from Photographs of the Sun's Glitter. *J. Opt. Soc. Am.* **1954**, *44*, 838–850. [\[CrossRef\]](#)
4. Warren, M.A.; Simis, S.G.H.; Martinez-Vicente, V.; Poser, K.; Bresciani, M.; Alikas, K.; Spyrakos, E.; Giardino, C.; Ansper, A. Assessment of atmospheric correction algorithms for the Sentinel-2A MultiSpectral Imager over coastal and inland waters. *Remote Sens. Environ.* **2019**, *225*, 267–289. [\[CrossRef\]](#)

5. Wang, J.; Wang, Y.; Lee, Z.; Wang, D.; Chen, S.; Lai, W. A revision of NASA SeaDAS atmospheric correction algorithm over turbid waters with artificial Neural Networks estimated remote-sensing reflectance in the near-infrared. *ISPRS J. Photogramm. Remote Sens.* **2022**, *194*, 235–249. [[CrossRef](#)]
6. Tanre, D.; Herman, M.; Deschamps, P. Y.; de Lefle, A. Atmospheric modeling for space measurements of ground reflectances, including bidirectional properties. *Appl. Opt.* **1979**, *18*, 3587–3594. [[CrossRef](#)]
7. Putsay, M. A simple atmospheric correction method for the short wave satellite images. *International J. Remote Sens.* **1992**, *13*, 1549–1558. [[CrossRef](#)] [[PubMed](#)]
8. Berk, A.; Adler-Golden, S.M.; Ratkowski, A.J.; Felde, G.W.; Anderson, G.P.; Hoke, M.L.; Cooley, T.; Chetwynd, J.H.; Gardner, J.A.; Matthew, M.W.; et al. Exploiting MODTRAN radiation transport for atmospheric correction: The FLAASH algorithm. In Proceedings of the Fifth International Conference on Information Fusion. FUSION 2002 (IEEE Cat.No.02EX5997), Annapolis, MD, USA, 8–11 July 2002; pp. 798–803. [[CrossRef](#)]
9. Vermote, E.F.; Vermeulen, A. Atmospheric Correction Algorithm: Spectral Reflectances (MOD09). Algorithm Theoretical Background Document, Version 4.0. 1999. Available online: http://modis.gsfc.nasa.gov/data/atbd/atbd_mod08.pdf (accessed on 30 January 2023). [[CrossRef](#)]
10. Lyapustin, A.; Wang, Y.; Korin, S.; Huang, D. MODIS Collection 6 MAIAC algorithm. *Atmos. Meas. Tech.* **2018**, *11*, 5741–5765.
11. Reinersman, P.N.; Carder, K.L. Monte Carlo simulation of the atmospheric point-spread function with an application to correction for the adjacency effect. *Appl. Opt.* **1995**, *34*, 4453–4471.
12. Katkovsky, L.V.; Martinov, A.O.; Siliuk, V.A.; Ivanov, D.A.; Kokhanovsky, A.A. Fast Atmospheric Correction Method for Hyperspectral Data. *Remote Sens.* **2018**, *10*, 1698. [[CrossRef](#)]
13. Shi, H.; Xiao, Z. The 4SAILT Model: An Improved 4SAIL Canopy Radiative Transfer Model for Sloping Terrain. *IEEE Trans. Geosci. Remote Sens.* **2021**, *59*, 5515–5525. [[CrossRef](#)]
14. Tanre, D.; Holben, B.N.; Kaufman, Y.J. Atmospheric correction algorithm for NOAA-AVHRR products: theory and application. *IEEE Trans. Geosci. Remote Sens.* **1992**, *30*, 231–248. [[CrossRef](#)]
15. Zimovaya, A.V.; Tarasenkov, M.V.; Belov, V.V. Radiation Polarization Effect on the Retrieval of the Earth’s Surface Reflection Coefficient from Satellite Data in the Visible Wavelength Range. *Atmos. Ocean. Opt.* **2018**, *31*, 131–136. [[CrossRef](#)]
16. Kotchenova, S.Y.; Vermote, E.F.; Matarrese, R.; Klemm, F.J. Validation of a vector version of the 6S radiative transfer code for atmospheric correction of satellite data. Part I: Path radiance. *Appl. Opt.* **2006**, *45*, 6762–6774. [[CrossRef](#)]
17. Cahalan, R.F.; Oreopoulos, L.; Wen, G.; Marshak, A.; Tsay, S.-C.; DeFelice, T. Cloud characterization and clear-sky correction from Landsat-7. *Remote Sens. Environ.* **2002**, *78*, 83–98. [[CrossRef](#)]
18. Wen, G.; Marshak, A.; Cahalan, R.F.; Remer, L.A.; Kleidman, R.G. 3-D aerosol-cloud radiative interaction observed in collocated MODIS and ASTER images of cumulus cloud fields. *J. Geophys. Res.* **2007**, *112*, D13204. [[CrossRef](#)]
19. Varnai, T.; Marshak, A. MODIS observations of enhanced clear sky reflectance near clouds. *Geophys. Res. Lett.* **2009**, *36*, L06807. [[CrossRef](#)]
20. Marshak, A.; Evans, K.F.; Varnai, T.; Wen, G. Extending 3D near-cloud corrections from shorter to longer wavelengths. *J. Quant. Spectrosc. Radiat. Transf.* **2014**, *147*, 79–85. [[CrossRef](#)]
21. Tarasenkov, M.V.; Engel, M.V.; Zonov, M.N.; Belov, V.V. Assessing the Cloud Adjacency Effect on Retrieval of the Ground Surface Reflectance from MODIS Satellite Data for the Baikal Region. *Atmosphere* **2022**, *13*, 2054. [[CrossRef](#)]
22. Richter, R.; Schläpfer, D. *ATCOR-2/3 User Guide*; ReSe Applications Schläpfer: Wil, Switzerland, 2012; p. 203. [[CrossRef](#)]
23. Miller, Craig J. Performance assessment of ACORN atmospheric correction algorithm. In Proceedings of the SPIE 4725, Algorithms and Technologies for Multispectral, Hyperspectral, and Ultraspectral Imagery VIII, AeroSense 2002, Orlando, FL, USA, 2 August 2002. [[CrossRef](#)]
24. Gao, B.-C.; Heidebrecht, K.B.; Goetz, A.F.H. *Atmosphere Removal Program (ATREM) Version 3.1 Users Guide*; Center for the Study of Earth from Space (CSES), Cooperative Institute for Research in Environmental Sciences (CIRES), University of Colorado: Boulder, CO, USA, 1996. [[CrossRef](#)]
25. Adler-Golden, S.M.; Matthew, M.W.; Bernstein, L.S.; Levine, R.Y.; Berk, A.; Richtsmeier, S.C.; Acharya, P.K.; Anderson, G.P.; Felde, J.W.; Gardner, J.A.; et al. Atmospheric correction for shortwave spectral imagery based on MODTRAN4. *Proc. SPIE Imaging Spectrom. V* **1999**, 3753. [[CrossRef](#)]
26. Qu, Z.; Kindel, B.C.; Goetz, A.F.H. The High Accuracy Atmospheric Correction for Hyperspectral Data (HATCH) model. *IEEE Trans. Geosci. Remote Sens.* **2003**, *41*, 1223–1231. [[CrossRef](#)]
27. Tarasenkov, M.V.; Zimovaya, A.V.; Belov, V.V.; Engel, M.V. Retrieval of Reflection Coefficients of the Earth’s Surface from MODIS Satellite Measurements Considering Radiation Polarization. *Atmos. Ocean. Opt.* **2020**, *33*, 179–187.
28. Cerasoli, S.; Campagnolo, M.; Faria, J.; Nogueira, C.; Caldeira, M.D.C. On estimating the gross primary productivity of Mediterranean grasslands under different fertilization regimes using vegetation indices and hyperspectral reflectance. *Biogeosciences* **2018**, *15*, 5455–5471. [[CrossRef](#)]
29. Vermote, E.; Justice, C.O.; Breon, F.-M. Towards a Generalized Approach for Correction of the BRDF Effect in MODIS Directional Reflectances. *IEEE Trans. Geosci. Remote Sens.* **2009**, *47*, 898–908.
30. Roujean, J.-L.; Leroy, M.; Deschamps, P.-Y. A bidirectional reflectance model of the Earth’s surface for the correction of remote sensing data. *J. Geophys. Res.* **1992**, *97*, 20455–20468. [[CrossRef](#)]

31. Rahman, H.; Pinty, B.; Verstraete, M.M. Coupled surface-atmosphere reflectance (CSAR) model: 2. Semiempirical surface model usable with NOAA advanced very high resolution radiometer data *J. Geophys. Res.* **1993**, *98*, 20791–20801. [[CrossRef](#)]
32. Verhoef, W.; Bach, H. Remote sensing data assimilation using coupled radiative transfer models. *Phys. Chem. Earth Parts A/B/C* **2003**, *28*, 3–13. [[CrossRef](#)]
33. Maignan, F.; Breon, F.-M.; Lacaze, R. Bidirectional reflectance of Earth targets: evaluation of analytical models using a large set of spaceborne measurements with emphasis on the Hot Spot. *Remote Sens. Environ.* **2004**, *90*, 210–220. [[CrossRef](#)]
34. Mousivand, A.; Verhoef, W.; Menenti, M.; Gorte, B. Modeling Top of Atmosphere Radiance over Heterogeneous Non-Lambertian Rugged Terrain. *Remote Sens.* **2015**, *7*, 8019–8044. [[CrossRef](#)]
35. Jia, W.; Pang, Y.; Tortini, R.; Schlapfer, D.; Li, Z.; Roujean, J.-L. A Kernel-Driven BRDF Approach to Correct Airborne Hyperspectral Imagery over Forested Areas with Rugged Topography *Remote Sens.* **2020**, *12*, 33. [[CrossRef](#)]
36. NOAA National Centers for Environmental Information. 2022: ETOPO 2022 15 Arc-Second Global Relief Model. NOAA National Centers for Environmental Information. Available online: https://data.noaa.gov/metaview/page?xml=NOAA/NESDIS/NGDC/MGG/DEM//iso/xml/etopo_2022.xml&view=getDataView&header=None (accessed on 30 January 2023). [[CrossRef](#)]
37. Supplementary Material. Available online: https://github.com/MarinaEngel/Atmosphere_2023 (accessed on 31 January 2023). [[CrossRef](#)]
38. Tarasenkov, M.V.; Belov, V.V.; Engel, M.V. Algorithm for reconstruction of the Earth surface reflectance from Modis satellite measurements in a turbid atmosphere. In Proceedings of the SPIE 10833, 24th International Symposium on Atmospheric and Ocean Optics: Atmospheric Physics, Tomsk, Russia, 2–5 July 2018; Volume 10833, pp. 1–16. [[CrossRef](#)]
39. Kneizys, F.X.; Robertson, D.C.; Abreu, L.W.; Acharya, P.; Anderson, G.P.; Rothman, L.S.; Chetwynd, J.H.; Selby, J.E.A.; Shettle, E.P.; Gallery, W.O.; et al. *The MODTRAN 2/3 Report and LOWTRAN 7 Model*; U.S. Air Force Geophysics Laboratory: Hanscom, MA, USA, 1996. [[CrossRef](#)]
40. Bucholtz, A. Rayleigh-scattering calculations for the terrestrial atmosphere. *Appl. Opt.* **1995**, *34*, 2765–2773. [[CrossRef](#)]
41. HITRAN Database. Available online: <https://hitran.org/> (accessed on 30 January 2023). [[CrossRef](#)]
42. Belov, V.V.; Tarasenkov, M.V. Statistical Modeling of the Point Spread Function in the Spherical Atmosphere and a Criterion for Detecting Image Isoplanarity Zones. *Atmos. Ocean. Opt.* **2010**, *23*, 441–447. [[CrossRef](#)]
43. Marchuk, G.I.; Mikhailov, G.A.; Nazarialiev, M.A.; Darbinjan, R.A.; Kargin, B.A.; Elepov, B.S. *The Monte Carlo Methods in Atmospheric Optics*; Springer: Berlin/Heidelberg, Germany, 1980. [[CrossRef](#)]
44. Coulson, K.; Dave, J.; Sekera, Z. *Tables Related to Radiation Emerging from a Planetary Atmosphere with Rayleigh Scattering*; University of California Press: Berkeley, CA, USA, 1960; pp. 56–58.
45. Mekler, Y.; Kaufman, Y.J. Contrast reduction by the atmosphere and retrieval of nonuniform surface reflectance. *Appl. Opt.* **1982**, *21*, 310–316.
46. Lenoble, J. *Radiative Transfer in Scattering and Absorbing Atmospheres: Standard Computational Procedures*; Deepak, A., Ed.; American Meteorological Society: Boston, MA, USA, 1985; 314.
47. Lenoble, J. Modeling of the Influence of Snow Reflectance on Ultraviolet Irradiance for Cloudless Sky. *Appl. Opt.* **1998**, *37*, 2441–2447.
48. International Working Group on Polarized Radiative Transfer (IPRT). Available online: <https://www.meteo.physik.uni-muenchen.de/~iprt/doku.php?id=start> (accessed on 30 January 2023). [[CrossRef](#)] [[PubMed](#)]
49. Radiometric Calibration Network Portal. Available online: <https://www.radcalnet.org/> (accessed on 30 January 2023).

Disclaimer/Publisher’s Note: The statements, opinions and data contained in all publications are solely those of the individual author(s) and contributor(s) and not of MDPI and/or the editor(s). MDPI and/or the editor(s) disclaim responsibility for any injury to people or property resulting from any ideas, methods, instructions or products referred to in the content.